Modeling Analysis of an Actively Cooled Scramjet Combustor Under Different Kerosene/Air Ratios

Wei Yao,* Yang Lu,† Kun Wu,‡ Jing Wang,§ and Xuejun Fan¶

Chinese Academy of Sciences, 100190 Beijing, People's Republic of China

Improved delayed detached Eddy simulation (IDDES) modeling based on a developed skeletal combustion mechanism of kerosene/air is conducted for a full-scale actively cooled scramjet combustor under two different global equivalence ratios. A reformulated partially stirred reactor (PaSR) is proposed to adapt it for high mesh resolution. A skeletal mechanism consisting of only 28 species and 92 reactions is reduced for the kerosene combustion modeling. A one-dimensional solid-gas-liquid coupling method is developed to simulate the active cooling effect. The time-averaged static pressure and wall heat flux profiles are well predicted for both fuel-lean and stoichiometric cases. The supersonic flow, mixing, and combustion characteristics under the two fuel/air ratios are quantitatively compared based on the efficiency indices, Takeno Flame Index, and the correlation statistics between heat release rate and mixture fraction. The vorticity and its evolution are analyzed through the five source terms for the two cases. The turbulence-chemistry interaction is then analyzed by the aid of numerous quantitative indices, such as Damköhler number, PaSR coefficient, and scalar dissipation rate, as well as their correlation statistics to identify the main combustion modes in the scramjet combustor.

Nomenclature

A	=	cross-sectional area
C_{mix}	=	model constant
C_p	=	specific heat, J/(kg·K)
c_i	=	molar concentration of species i, mol/m^3
c_k	=	model constant
c_α	=	molar concentration of species α, mol/m^3
Da	=	Damköhler number
D_α, D_T	=	mass and thermal diffusivity, m^2/s
dQ	=	heat release rate, W
d_{IDDES}	=	length scale in IDDES, m
E	=	constant in the near-wall log-law
H, H_t	=	absolute and total absolute enthalpy, J/kg
$k_{f,\beta}, k_{r,\beta}$	=	the forward and reverse rate constants of the βth-elementary reaction
k_t	=	turbulence kinetic energy, m^2/s^2
L, M, N	=	numbers of species, reactions, and mesh cell
l_k	=	Kolmogorov length scale, m
Ma	=	Mach number
τ_c	=	fuel mass flow rates, kg/s
Pr_t	=	turbulent Prandtl number
p, P_t	=	static and total pressure, Pa
$Q_{\text{air}}, Q_{\text{fuel}}$	=	flow rate of air crossflow or fuel jet, g/s
q_i	=	heat flux in the ith direction, W/m^2
$\dot{q}_w$	=	convective wall heat flux, W/m^2
R, R_u	=	gas constant (J/[kg · K]) and universal gas constant ($\approx$8.314 J/[mol · K])
r_d	=	squared ratio of model length scale to wall distance
S_{ij}	=	strain rate tensor, m/s
Sc_t	=	turbulent Schmidt number
T, T_t	=	static and total temperature, K
$\mathbf{u}, u_i, u_i'$	=	velocity vector, ith component and fluctuation, m/s
W	=	molecular weight, g/mol
x_i	=	Cartesian coordinate in direction i
Y	=	mass fraction
y^+	=	nondimensional wall distance
γ_α	=	third-body coefficient for species α
δ_l	=	flame thickness, m
ε	=	small quantity to avoid zero division, usually 1×10^{-30}
ϵ	=	turbulence dissipation rate, J/(kg·s)
η_{mix}	=	mixing efficiency
η_{comb}	=	combustion efficiency
η_{Pt}	=	total pressure loss
κ	=	von Kármán constant (0.4187)
κ_{PaSR}	=	partially stirred reactor coefficient
$\nu, \nu_t, \nu_{\text{eff}}$	=	kinematic, turbulent, and effective viscosity, m^2/s
ν_{CO_2}	=	stoichiometric coefficient of CO_2
$\nu_{\alpha,k}'', \nu_{\alpha,k}'$	=	forward and reverse stoichiometric coefficient of the kth reaction
$\xi, \widetilde{\xi'^2}$	=	mixture fraction and its variance
ρ	=	density, kg/m^3
$\tilde{\tau}_{ij}, \tau_{ij}$	=	viscous and Reynolds stress tensor, kg/(m·s^2)
$\tau_c,$	=	chemical time scales of chemistry, subgrid scale,
$\tau_\Delta, \tau_{\text{mix}}$	=	and micromixing, s
τ_k	=	Kolmogorov time scale, s
Φ	=	global equivalence ratio
$\tilde{\chi}$	=	mean scalar dissipation rate, s^{-1}
$\Psi_{T,j}$	=	turbulent enthalpy flux, W/m^2
$\Psi_{\alpha,j}$	=	turbulent species diffusion, kg/(m^2· s)
ω_α	=	mass production of species α, kg/(m^3·K)
$\mathbf{\Omega}, \mathbf{\Omega}_s$	=	vorticity (s^{-1}) and its source term (s^{-2})

Subscripts

air	=	quantity of the air crossflow
fuel	=	fuel quantity
i, j	=	direction indices
st	=	quantity at stoichiometric condition

*Associate Professor, Key Laboratory of High Temperature Gas Dynamics, Institute of Mechanics; also School of Engineering Science, University of Chinese Academy of Science, 100049 Beijing, People's Republic of China; weiyao@imech.ac.cn. Member AIAA.

†Associate Professor, Key Laboratory of High Temperature Gas Dynamics, Institute of Mechanics; luyang@imech.ac.cn.

‡Ph.D. Student, Key Laboratory of High Temperature Gas Dynamics, Institute of Mechanics; wukun@imech.ac.cn.

§Senior Engineer, Key Laboratory of High Temperature Gas Dynamics, Institute of Mechanics; wangjing@imech.ac.cn.

¶Professor, Key Laboratory of High Temperature Gas Dynamics, Institute of Mechanics; also School of Engineering Science, University of Chinese Academy of Science, 100049 Beijing, People's Republic of China; xfan@imech.ac.cn. Lifetime Member AIAA (Corresponding Author).

x_1	=	quantity at the streamwise location of x_1
α	=	species index
β	=	reaction index

Superscripts

~	=	Favre-averaged quantity
−	=	averaged quantity
∗	=	quantities corresponding to the reference enthalpy

I. Introduction

WITH the advance of computational resources, high-fidelity full-scale combustor modeling, especially those based on large Eddy simulation (LES), is of great help for the understanding of internal flow characteristics and the performance-based design of scramjet combustors. However, till now, only very few scramjet modelings are fueled by kerosene [1–3], whereas most of them are fueled by hydrogen (e.g., those based on HyShot I&II [4] or SCHOLAR cases [5]). Kerosene is a more practical choice for low-cost scramjets cruising at Mach numbers (Ma) between 4 and 8, which is the short-term goal of hypersonic flight in the next few decades. Thus, there is a more urgent need to understand the flow and combustion processes in kerosene-fueled scramjet combustors by the aid of high-fidelity modeling.

One of the main challenges in the modeling of kerosene-fueled scramjet combustor originates from the lack of reduced or skeletal mechanisms. Kerosene contains thousands of species, mostly in the molecular formula of C_7–C_{16}. Even using surrogate species, the detailed mechanisms still contain thousands of elementary reactions. The mechanisms used in previous kerosene-fueled supersonic combustion modeling [1–3] are mostly simple global or semikinetic mechanisms. To date, few reduced or skeletal kerosene mechanisms specially developed for supersonic combustion have been proposed in the literature. In this study, a skeletal mechanism consisting of only 28 species is proposed and validated.

In this study, a scramjet combustor working at a flight Ma of 6 is analyzed to extend the understanding of internal flow and combustion characteristics in the high-Ma regime ($Ma \geq 6$). Two modeling cases at different Φs (Φ, global equivalence ratio) are examined for comparison. To alleviate the computational cost in boundary-layer modeling, improved delayed detached eddy simulation (IDDES) [6] is employed. A solid-gas-liquid (SGL) coupled thermal analysis method is developed to model the heat transfer process associated with actively cooled units. Streamwise measurements of static pressure and wall heat flux are first used to validate the predictions. The time-averaged and instantaneous fields are then analyzed by the aid of numerous quantitative indices to gain an in-depth insight into the combined flow, mixing, and combustion processes.

II. Experimental Tests at Different Fuel/Air Ratios

A. Test Platform

The experimental tests were conducted in the long-time direct-connect supersonic combustion test facility at the Chinese Academy of Sciences. The whole platform consists of an air supply system, a nozzle section, a scramjet combustor assembly, a water-cooling system, a data acquisition/controlling system, and a fuel heating/delivery system. The full-scale scramjet combustor with consecutively connected isolator, burner, and expander sections (as schematically shown in Fig. 1) was modeled as a whole in this study. The combustor has a rectangular cross section with a spanwise width of 150 mm. The isolator is a constant area duct with

Fig. 1 Schematic of the scramjet combustor.

a height of 70 mm. The burner section has a length of 800 mm and a divergent angle of 2 deg on the upper wall. The expander section that acts as the exhaust nozzle has a length of 600 mm and a divergent angle of 5.3 deg on the upper wall. Supercritical kerosene and gaseous H_2 are injected perpendicular to the combustor airstream, respectively, through four upstream and four downstream injectors. The kerosene injectors have the same diameter of $D = 2.8$ mm and are located 56 mm before the leading edge of the upstream cavity. The H_2 injectors have the diameter of $D = 1$ mm and are located 8 mm before of the leading edge of the upstream cavity. The streamwise distance from the isolator inlet is 758.5 mm to the upstream fuel injector and 1108 mm to the downstream fuel injector. Hydrogen is used temporally for ignition and will be turned off after a definite pressure rise has been maintained for a period of 3 s. Static pressure and wall heat flux along the streamwise distance were recorded by pressure transmitters attached to the lateral wall and heat flux sensors attached to the upper and lower walls. The heat flux sensor based on the principle of Gardon heat flux gauge was re-designed by use of a recirculating water cooling system and a heat bypass system to extend its range for harsh supersonic combustion environments.

B. Case Configurations

Table 1 summarizes the test configurations, all with incoming air stream corresponding to a flight Ma of 6.0. The incoming vitiated air, which is supplied by burning hydrogen in the air with oxygen replenishment, has a raised stagnation temperature close to 1700 K and a Ma of 2.5 on the inlet of the isolator. The mass flow rates of hydrogen, oxygen, and air into the preburner are listed in Table 1 and the final composition of vitiated air is N_2 in 59.0% (volume fraction), O_2 in 20.6%, and H_2O in 20.4%. The incoming crossflow condition of vitiated air is kept the same. The RP-3 kerosene, which changes its equivalence ratio from 0.6 to 1.0, is preheated to above its critical temperature of 630 K before the injection. The hydrogen jet, which has a small equivalence ratio of 0.1, is used only for the ignition and will be shut off far before the data acquisition. Therefore, the actual global equivalence ratio represented by symbol Φ changes from 0.6 to 1.0 in the two examined cases. The equivalence ratio is equally split between the upstream and the downstream injectors for both the hydrogen and RP-3 streams.

III. Numerical Models

A. The Flow Solver: AstroFoam

The modeling is performed by the compressible reacting flow solver AstroFoam, which is developed on the basis of the compressible flow solver rhoCentralFoam distributed with Open-FOAM V3.0.1 CFD package [7] mainly through adding the functions of multispecies transport and multicomponent reaction. The major developments adopted in this study include 1) JANAF thermophysical properties and multicomponent diffusivities calculated by the CHEMKIN-II package [8]; 2) skeletal kerosene mechanism used to calculate the multicomponent reaction rates; 3) in situ adaptive tabulation (ISAT) [9] method to speed up the costly stiff chemistry solving; 4) 1-D SGL coupling heat transfer code to estimate the thermal boundary condition on the combustor walls embedded by cooling channels; 5) absolute/sensible enthalpy equation instead of the sensible internal energy equation is solved for transient reacting flows; and 6) dynamic load balancing technique to redistribute the computational load among processors.

The inviscid convective fluxes in AstroFoam inherited from rhoCentralFoam are evaluated by the semidiscrete central Kurganov–Tadmor (KT) scheme [10,11], which assumes a low numerical dissipation in resolving discontinuities (e.g., shock waves and rarefaction tips) yet a high computational efficiency due to its Riemann-free simplicity. The numerical viscosity of the central KT scheme is of order $\sim O(\Delta x^3)$, and thus oscillation may occur near shock waves. To damp the unphysical oscillation, total variation diminishing (TVD)/normalized variable diagram (NVD) families of discretization schemes with different flux limiters (e.g., Minimod, SFCD, Vanleer, Superbee, and Gamma) are tested and the Minimod
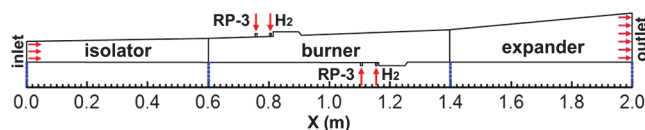
Table 1 Test case configurations

Vitiated air crossflow						Kerosene injection				Injectors
$P_{t,\text{air}}$, MPa	$T_{t,\text{air}}$, K	Q_{air}, g/s	Q_{H2}, g/s	Q_{O2}, g/s	Ma	$P_{t,\text{fuel}}$, MPa	$T_{t,\text{fuel}}$, K	Q_{fuel}, g/s	Φ	Location
0.811	1701	2020.4	37.9	461.6	2.5	3.24	771	112.7	0.6	Upstream + downstream
0.800	1686	2047.9	39.0	463.9		3.77	764	132.4	1.0	

limiter shows the best numerical stability among the second-order TVD/NVD schemes. The potential ingredient that causes numerical oscillations in the KT central scheme is the midpoint quadrature rule for the temporal integration of the numerical fluxes. Especially for semidiscrete central scheme, a small time step $\Delta t \to 0$ is required to inhibit any unphysical numerical flux. In the calculation, the time step is limited both by a maximum Courant number of 0.2 and a user-specified maximum time step of 5×10^{-8} s to avoid the spurious oscillations. In addition, restrictions on density, velocity, species mass fraction, and temperature fields are implemented to avoid the divergence caused by occasional unphysical values.

AstroFoam, together with the original rhoCentralFoam solver, was first validated for various frozen flows, including the canonical shock tube problem, forward step flow, hypersonic flow over a biconic, and supersonic jets [11–14]. The solver is then applied to different types of scramjet combustor cases [15–17] to examine its accuracy and robustness in the engineering modeling of supersonic combustion.

B. Governing Equations

The unsteady and three-dimensional Favre-averaged compressible Navier–Stokes equations are solved for multicomponent reactive gas mixtures, which are represented by a set of conservative variables $(\bar{\rho}, \tilde{u}_i, \tilde{H}_t, \tilde{Y}_\alpha)$,

$$\frac{\partial \bar{\rho}}{\partial t} + \frac{\partial \bar{\rho} \tilde{u}_j}{\partial x_j} = 0 \tag{1}$$

$$\frac{\partial \bar{\rho} \tilde{u}_i}{\partial t} + \frac{\partial \bar{\rho} \tilde{u}_j \tilde{u}_i}{\partial x_j} + \frac{\partial \bar{p}}{\partial x_j} - \frac{\partial \tilde{\tau}_{ij}}{\partial x_j} = -\frac{\partial ij}{\partial x_j} \tag{2}$$

$$\frac{\partial \bar{\rho} \tilde{H}_t}{\partial t} + \frac{\partial \bar{\rho} \tilde{u}_j \tilde{H}_t}{\partial x_j} - \frac{\partial}{\partial x_j}\left(\bar{\rho} D_T \frac{\partial \tilde{H}_t}{\partial x_j}\right) - \frac{\partial \bar{p}}{\partial t} - \frac{\partial \tilde{u}_j \tilde{\tau}_{ij}}{\partial x_j} = -\frac{\partial \Psi_{T,j}}{\partial x_j} \tag{3}$$

$$\frac{\partial \bar{\rho} \tilde{Y}_\alpha}{\partial t} + \frac{\partial \bar{\rho} \tilde{u}_j \tilde{Y}_\alpha}{\partial x_j} - \frac{\partial}{\partial x_j}\left(\bar{\rho} D_\alpha \frac{\partial \tilde{Y}_\alpha}{\partial x_j}\right) = -\frac{\partial \Psi_{\alpha,j}}{\partial x_j} + \bar{\omega}_\alpha \tag{4}$$

$$\bar{p} = \bar{\rho} R \tilde{T} \tag{5}$$

$$\tilde{H}_t = \tilde{H}^0 + \int_0^T C_p \, dT + \frac{1}{2} \tilde{u}_i \tilde{u}_i \tag{6}$$

Here the bar ($-$) and the tilde ($\sim$) represent averaged- or Favre-averaged quantities, respectively, t denotes the time, x_i is the Cartesian coordinate in direction i, $\bar{\rho}$ is the density, $\tilde{u}_i$ is the velocity component in x_i direction (spatial dimension $i = 1, 2, 3$), $\bar{p}$ is the pressure, $\tilde{\tau}_{ij}$ is the viscous stress tensor, $\tilde{H}_t = \tilde{H} + 0.5\tilde{u}_i^2$ is the total absolute enthalpy obtained as the sum of the absolute enthalpy $\tilde{H}$ and the resolved kinetic energy, $\tilde{H}^0$ is the formation enthalpy, q_i is the heat flux vector in the ith direction, $\tilde{Y}_\alpha$ is the mass fraction of species α ($\alpha = 1, \ldots, L$, where L is the total species number), the specific heat C_p is a function of species concentrations and temperature, $\bar{\omega}_\alpha$ is the averaged mass production rate of chemical species α in the unit of $\text{kg} \cdot \text{m}^{(-3)} \cdot \text{s}^{-1}$, D_α is mixture-averaged mass diffusivity of species α, D_T is the thermal diffusivity, $\tilde{T}$ is the temperature, $R = R_u/W$ is the gas constant, $R_u = 8.314 \ \text{J} \cdot \text{mol}^{-1} \cdot \text{K}^{-1}$ is the universal gas

constant, and $W = (\sum_{k=1}^N Y_\alpha/W_\alpha)^{-1}$ is the molar weight of the multicomponent mixture. The computable averaged momentum diffusive flux is given by

$$\tilde{\tau}_{ij} = \bar{\rho} \nu(\tilde{T})\left(2\tilde{S}_{ij} - \frac{2}{3}\delta_{ij}\tilde{S}_{kk}\right) \tag{7}$$

which depends on the computable strain-rate tensor of the resolved scales

$$\tilde{S}_{ij} = \frac{1}{2}\left(\frac{\partial \tilde{u}_i}{\partial x_j} + \frac{\partial \tilde{u}_j}{\partial x_i}\right) \tag{8}$$

The Reynolds stresses (τ_{ij}) and turbulent fluxes ($\Psi_{T,j}$ and $\Psi_{\alpha,j}$) in Eqs. (1–6) are unclosed and require specific modeling. The Reynolds stress, defined as $\tau_{ij} = \bar{\rho}(\widetilde{u_i u_j} - \tilde{u}_i \tilde{u}_j)$, is modeled by Boussinesq eddy viscosity hypothesis, where the Reynolds stresses are taken to be proportional to the local stain rate of the resolved flow,

$$\tau_{ij} = -2\bar{\rho}\nu_t \tilde{S}_{ij} + \frac{2}{3}\delta_{ij}\bar{\rho} k_t \tag{9}$$

where ν_t is the eddy viscosity given by an approximate turbulence model and is the unresolved turbulence kinetic energy. The turbulent enthalpy flux term $\Psi_{T,j} = \bar{\rho}(\widetilde{u_j H_t} - \tilde{u}_j \tilde{H}_t)$ is modeled by a gradient diffusion assumption as

$$\Psi_{T,j} = -2\bar{\rho}\frac{\nu_t}{Pr_t}\frac{\partial \tilde{H}_t}{\partial x_j} \tag{10}$$

where Pr_t is the turbulent Prandtl number. The turbulent species diffusion term $\Psi_{\alpha,j} = \bar{\rho}(\widetilde{u_j Y_\alpha} - \tilde{u}_j \widetilde{Y_\alpha})$ is also modeled using the gradient diffusion assumption as

$$\Psi_{\alpha,j} = -2\bar{\rho}\frac{\nu_t}{Sc_t}\frac{\partial \tilde{Y}_\alpha}{\partial x_j} \tag{11}$$

where Sc_t is the turbulent Schmidt number.

The Favre-filtered or Favre-averaged Navier–Stokes equations including transport equations for individual species and absolute enthalpy are solved in a uniform framework by equally treating the turbulent viscosity in the Reynolds-averaged Navier–Stokes (RANS) mode and the subgrid scale (SGS) viscosity in the LES mode. The numerical treatments in resolving Eqs. (1–11) are the same for any turbulence models, and the switch between RANS and LES is determined by which turbulence model the eddy viscosity is calculated.

The thermodynamic and transport properties of the gas mixture, such as the absolute enthalpy, the specific heat, the viscosity, the thermal, and mass diffusivities, are calculated using the chemical kinetics package CHEMKIN-II [8] based on the JANAF thermophysical table and a CHEMKIN-format transport database. The viscosity, specific heat, and conductivity are all independent of pressure but only depend on temperature. The mixture-averaged viscosity and thermal conductivity are calculated using the modified Wilke's law [18] and the combination averaging, respectively. Mixture-averaged mass diffusivities are used, and the mass conservation is achieved by setting the nitrogen as inert gas, whose mass fraction is computed simply by subtracting the sum of the

remaining mass fractions from unity. The thermal diffusivity is estimated as ν/Pr with a unity laminar Prandtl number ($Pr = 1.0$).

C. Turbulence Modeling

To reduce the computational cost in modeling the wall boundary layers, a hybrid RANS/LES technique known as IDDES [6] is applied. The background RANS model is one-equation Spalart–Allmaras (S-A) model [19], which is used only in the modeling of wall boundary layers. The model contains a wall destruction term to reduce the turbulent viscosity in the laminar sublayer and logarithmic sublayer, providing a smooth transition from laminar to turbulent statuses. In IDDES, the subgrid length scale is redefined to be dependent not only on local cell sizes but also on the wall distance, and then a shielding function is used to avoid an excessively low subgrid viscosity deteriorating the detection of the boundary-layer edge. Such a treatment ensures that the RANS mode can fully cover the boundary layer.

D. Turbulent Combustion Modeling: A Reformulated PaSR Model

The turbulence-chemistry interaction is accounted for by the partially stirred reactor (PaSR) model [20]. In PaSR, the final reaction rate averaged reaction rate $\bar{\omega}_\alpha$ is determined by the characteristic time scales of chemistry (τ_c) and micro-mixing (τ_{mix}),

$$\bar{\omega}_\alpha = \frac{\tau_c}{\tau_c + \tau_{\text{mix}}} \omega_\alpha \qquad (12)$$

where τ_c is the chemical time scale and ω_α is the reaction rate over the current integration time step calculated from the Arrhenius law:

$$\omega_\alpha = \sum_{\beta=1}^{M} \omega_{\alpha,\beta} = \sum_{\beta=1}^{M} W_\alpha(\nu''_{\alpha,\beta} - \nu'_{\alpha,\beta})\left(k_{f,\beta}\prod_{\alpha=1}^{L}[c_\alpha]^{\nu'_{\alpha,\beta}} - k_{r,\beta}\prod_{\alpha=1}^{L}[c_\alpha]^{\nu''_{\alpha,\beta}}\right) \qquad (13)$$

Here, $\nu''_{\alpha,\beta}$ and $k_{f,\beta}$, respectively, indicate the forward stoichiometric coefficient and the forward rate constant of the βth-elementary reaction, whereas $\nu'_{\alpha,\beta}$ and $k_{r,\beta}$ are their reverse counterparts, and L and M are, respectively, the total numbers of species and elementary reactions. The rate constants follow the Arrhenius law with the Arrhenius coefficients given in the Appendix and c_α is the molar concentration of species α. To speed up the direct integration (DI) of the stiff chemistry, ISAT method [9] is used.

As an eddy break-up/dissipation-type model, PaSR assumes that reactions occur in well-mixed small-scale eddies (named fine structures), thereby the chemical reactions are constrained by the break-up/dissipation rate of large-scale eddies into small-scale eddies. The overall micromixing rate is determined by the turbulent mixing followed by the molecular diffusion as $\tau_{\text{mix}} = \tau_{\text{mix},t} + \tau_{\text{mix},l}$. Usually, an assumption is made that the molecular mixing within each cell is infinitely fast, and thus only the turbulent mixing is considered $\tau_{\text{mix}} \approx \tau_{\text{mix},t}$. The turbulent mixing time scale can be defined as the geometric mean of Kolmogorov time scale τ_k and the largest unresolved eddy time scale [21] or the Taylor time scale τ_t if the whole spectrum of time scales is considered [22]. In LES, the Taylor time scale can be replaced by SGS time scale τ_Δ [23], and then the turbulent mixing time scale is reformulated in this study as $\tau_{\text{mix},t} = \sqrt{\tau_k \tau_\Delta}$. Here $\tau_\Delta = k_t/\epsilon = (\nu_t/C_\mu\epsilon)^{1/2}$ with the constant $C_\mu = 0.09$, then

$$\tau_{\text{mix},t} = \frac{1}{C_\mu^{1/2}}\left(\frac{\sqrt{\nu \cdot \nu_t}}{\epsilon}\right)^{1/2} \qquad (14)$$

The reformulation is to adapt the generic PaSR model for modelings with high mesh resolution. Under laminar or well-resolved DNS-level resolutions, $\nu_t = 0$, then $\tau_{\text{mix},t} = 0$, and thus $\bar{\omega}_\alpha \to \omega_\alpha$, which turns the model back to be the laminar combustion model.

In the S-A model–based IDDES, the unresolved turbulence kinetic energy k_t and its dissipation rate ϵ are estimated from their relations

with turbulent viscosity ν_t, that is, $k_t = (\nu_t/(c_k d_{\text{IDDES}}))^2$ and $\epsilon = 2\nu_{\text{eff}}|S_{ij}|^2$, with $\nu_{\text{eff}} = \nu_t + \nu$, and $c_k = 0.07$. Usually, the characteristic chemical time scale is calculated as the reciprocal of Jacobian matrix $(\partial(\omega_\alpha/W_\alpha)/\partial c_i)^{-1}$, which will result in a τ_c essentially the same with $c_\alpha/(\omega_\alpha/W_\alpha)$, where c_α is molar concentration and ω_α is reaction rate of species α [24]. Because different elementary reactions can have extremely different chemical time scales varying by orders of magnitude, it is difficult to precisely define an overall chemical time scale for multicomponent mixtures. In this study, the overall chemical time scale is estimated as the ratio of the summation of species concentrations to that of reaction rates $\tau_c = \sum c_\alpha/\max(\sum(\omega_\alpha^+/W_\alpha), \varepsilon)$, with ε a small quantity. Here the forward production rates are calculated by only considering the forward reactions and neglecting all their reverse counterparts.

E. Preliminary Validation of the Skeletal Kerosene Mechanism

The chemical mechanism reduction from the original detailed kerosene mechanism consisting of 2185 species and 8217 elementary reactions [25] is conducted using the DRGEPSA method [26], which is the combination of directed relation graph with error propagation (DRGEP) and sensitivity analysis (SA). In our previous study [15], a skeletal mechanism consisting of 39 species and 153 reactions is obtained. Further reaction path analysis and SA continue to reduce the mechanism into a smaller skeletal mechanism consisting of only 28 species and 92 reactions, which are listed in the Appendix. The kinetic properties of skeletal mechanisms are first validated in zero-dimensional (0-D) or 1-D reactors.

The kinetic properties between the two skeletal mechanisms (28s/92r, 39s/153r) and the original mechanism (2185s/8217r) are compared in Fig. 2. The adiabatic flame temperature, total heat release, and ignition delay were calculated in a closed homogeneous adiabatic reactor under a constant pressure of 1 atm. The initial mixture temperature varies from 1200 to 2400 K for each case in the parameter study. The starting gas mixture is a stoichiometric mixture of kerosene (28.8% iso-octane, 62.4% n-decane, 8.8% n-propylcyclohexane in mass fraction) and air (21% O_2 and 79% N_2). Within the initial temperature range of 1200–2400 K, the adiabatic flame temperatures predicted by the two skeletal mechanisms are almost the same, and both are close to the prediction by the original detailed mechanism. The validation of total heat release is often ignored in the modeling of unenclosed flames but is important for enclosure combustion modelings, because the heat addition usually determines the pressure rise ratio. From Fig. 2b, the total heat release calculated by the two skeletal mechanisms is in excellent agreement with that by the detailed mechanism.

One key aspect of the kinetics for the scramjet combustor modeling is the accurate prediction of ignition delay. Overprediction of the ignition delay will produce a longer preignition distance downstream the jet port, more distributed flame sheets (thicker reaction zones), and usually lower peak temperature. The variation of several species concentrations as a function of reaction time is shown in Fig. 2c, where it can be seen that the ignition time defined by the peak in CO concentration can approximate, although slightly shorter than, the equilibrium time of the homogeneous stoichiometric mixture of kerosene/air. Here the ignition is registered as the peak CO concentration. The relative error in ignition delay can be calculated based on the results from the detailed mechanism. From Fig. 2d, the ignition delay is even closer to the value calculated by the detailed mechanism for the 28-species skeletal mechanism than the 39-species one. As shown in Fig. 2e, the mean relative ignition delay error is 57.6% for the 28-species mechanism and 118.1% for the 39-species mechanism in the temperature range from 1200 to 2400 K. The reaction progress of large-molecule kerosene can be roughly divided into two stages, that is, the pyrolysis from large molecules to small-molecule hydrocarbons (e.g., CH_x, C_2H_x, and C_3H_x with x representing different hydrogen atom numbers) and then the oxidation of those small-molecule hydrocarbons. The pyrolysis is a much more complex process involving a larger number of reaction paths. In DRGEPSA, most of those pyrolysis reaction paths and their corresponding pyrolysis products are removed, causing the ignition
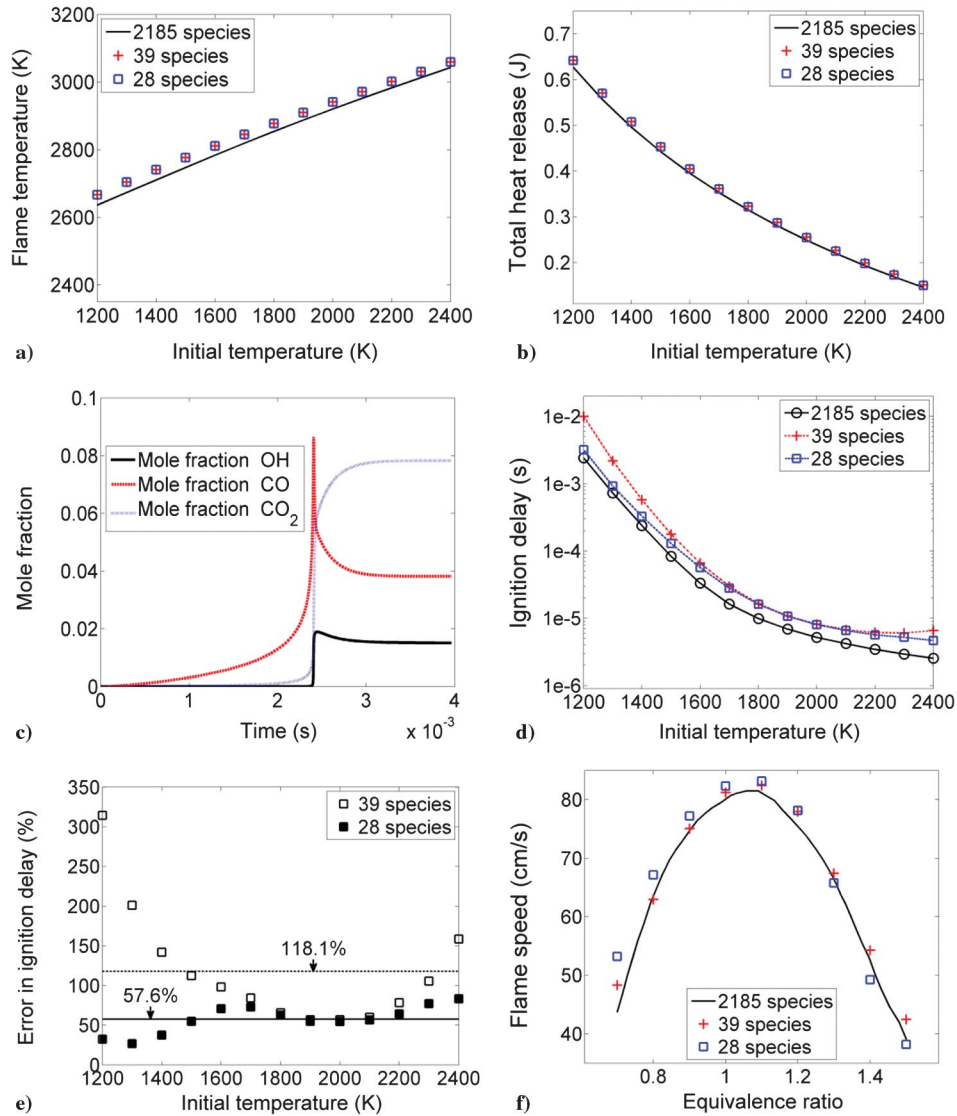
Fig. 2 **Comparison of kinetic properties for a) flame temperature, b) total heat release, c) time variation of species mole fractions, d) ignition delay in logarithmic scale, e) relative error in ignition delay, and f) laminar flame speed.**

process excessively delayed in the low-temperature regime. The 28-species mechanism performs better in the low-temperature regime probably because different pyrolysis reaction paths are selected.

The laminar flame speed is compared in Fig. 2f for an adiabatic, atmospheric-pressure, and stoichiometric kerosene-air mixture at an initial temperature of 473 K and Φ from 0.7 to 1.5. The premixed flame model solves a set of 1-D governing differential equations for continuity, species, and energy that describes the flame dynamics using an automatic coarse-to-fine grid refinement technique. Multicomponent diffusion is used by employing binary diffusivities. Unlike the 0-D homogeneous reactor, the chemical kinetics and transport processes are modeled together in the flame speed simulations. The agreement is better overall for the 39-species mechanism, whereas the 28-species mechanism slightly overpredicts the flame speed by up to 20% mainly under fuel-lean condition.

F. Computational Domain and Boundary Conditions

The computational domain shown in Fig. 1 contains the isolator, burner, and expander sections. Because of the bilateral symmetry of the combustor geometry and fuel injection layout, only a half-split combustor is modeled to save the computational cost. The spanwise variation of flow quantities in a full-domain modeling will be analyzed to assess the impact of such symmetry boundary condition in the future studies. The unstructured mesh is generated using the Cartesian CutCell method, which can produce high-quality uniform

hexahedral grid cells for most of the internal volume of the computational domain, while tetrahedron, wedge, or pyramid cells are filled only in large-curvature regions, for example, those near the borders or corners. The whole domain is meshed first with uniform 1 mm cells, which are then adaptively refined based on local curvatures and size functions. As shown in Fig. 3a, the mesh has been progressively refined around the injectors. Except in the boundary layer, the cells with a minimum size of 50 μm are distributed mainly around the fuel injectors, where the Kolmogorov scale is in a comparable size of around 50 μm estimated based on the fuel inlet properties. The inflation layer has an averaged thickness of 2 mm and contains 23 prism layers with the last prism located in the logarithmic layer. The initial prism layer height closest to the wall is 5 μm, which corresponds to a nondimensional wall distance (defined based on the friction velocity) $y^+ \sim o(1)$ on all the wall surfaces for the examined combustor flows. As shown in Fig. 3b, y^+ depends on the local kinematic viscosity and velocity gradient, which vary both spatially and temporally. To avoid the potential risk of y^+ extruding into the logarithmic layer locally, an extension of y^+-insensitive wall treatment is made to the S-A model through calculating the wall shear stress according to the log-law for nondimensional velocity

$$U^+ = \frac{1}{\kappa} l_n(Ey^+), \quad \text{if } y^+ > y_l^+ \qquad (15)$$
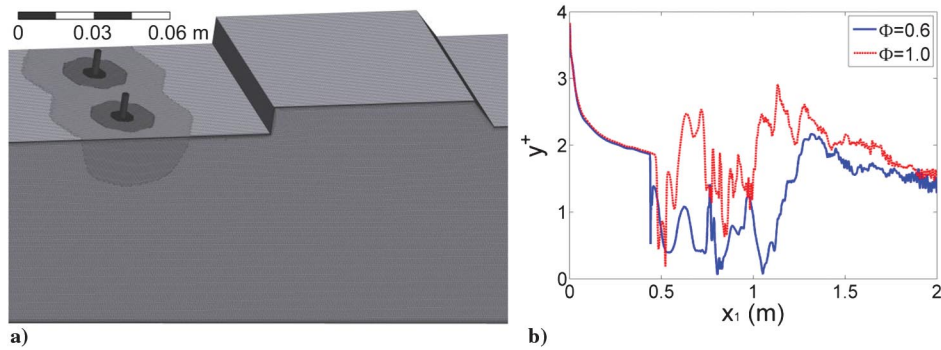
Fig. 3   a) Mesh distribution around the injectors, and b) the instantaneous y^+ profiles.

Here y_l^+ is determined by the constant $E = 9.8$ and $\kappa = 0.4187$ through solving $y_l^+ = (1/\kappa) \ln(Ey_l^+)$. In this study, the total cell number in the half-split combustor domain is 55.98 million. Grid quality analysis shows that 99.98% of the volume is meshed by hexahedral cells, 98.25% of the volume has a skewness smaller than 0.1, and 97.57% of the volume has an orthogonal quality higher than 0.99. The coordinate origin is located on the isolator inlet plane and x_1 denotes the streamwise direction.

Fixed pressure, temperature, and velocity are set on the isolator inlet and the fuel inlets according to those listed in Table 1. Because the inflow conditions of the air crossflow vary slightly in the experimental tests, averaged values are used. The principle of extended corresponding states (ECS) for RP-3 kerosene [27] is used to calculate the initial fuel properties because the compressibility of supercritical RP-3 cannot be described by the ideal gas equation. A RANS-type turbulent inlet boundary condition is specified on the isolator inlet by fixing the turbulence viscosity as $\nu_t/\nu = 1$. Open boundary condition is applied to the expander outlet, where zero gradient is used for outflow and ambient flow conditions for temperature and gas composition are specified should back-flow occur.

The inner wall temperature along the streamwise direction is estimated by the 1-D SGL coupled thermal analysis model. In the experimental tests, active cooling using external water is used to protect the combustor shells. The coupled heat transfer processes involving SGL phases shown in Fig. 4 were modeled [28], that is, the flow and combustion in the internal flow path, the heat conduction within the shells, and the heat transfer inside the cooling channels. The channel wall is a two-sided wall that forms the interface between the coolant fluid and the solid combustor shell body, and thus the thermal boundary conditions of the two regions are coupled. To simplify the analysis, 1-D parabolic equations of mass, momentum, and energy are solved iteratively for the internal combustor flow path and each cooling channel in a consecutive manner from the upstream to the downstream. Measured static pressure is used as the input to

Fig. 4   Schematic of the SGL-coupled heat transfer processes (down), and the inner wall temperatures (up).

save the iterative calculation in solving the momentum and continuity equations. The effects of variable geometry cross section, wall friction, heat, and mass addition are integrated through changing the local control volume and adding source terms to the equations. The final steady inner wall temperature profiles adjacent to the hot combustion gas calculated by the SGL-coupled heat transfer code are also shown in Fig. 4. As seen, the wall temperature varies between 430 and 520 K and increases slowly toward the expander exit. The inner wall temperature is slightly higher for the higher Φ. The estimated wall temperature is then explicitly set as the wall temperature in the 3-D IDDES modelings to simulate the active-cooling effect. The modeled wall heat flux in the 3-D IDDES modelings are calculated as

$$\dot{q}_w = \rho_w \alpha_w \left(\frac{\partial h}{\partial n}\right)_w \tag{16}$$

where ρ_w, α_w, and $(\partial h/\partial n)_w$ are the density, thermal diffusivity, and enthalpy gradient in the fluid side.

The parallel computations are performed at the national supercomputer center in Tianjin (TH-1) using 400 CPU cores for each case. The flush through time (FTT) defined based on the length of the combustor flow-path length (2 m) and the inlet flow speed of the vitiated air crossflow (1472 m/s) is 1.36×10^{-3} s. Each modeling case costs about 2×400 CPU months to ensure at least 3 FTTs for data sampling and statistics before another 3 FTTs to reach a quasi-steady flow status.

IV.   Results and Discussion

A.   Supersonic Flow, Mixing, and Combustion Characteristics

First, a grid SA is conducted for both the cases under a total of five mesh sets: 18.54 million/1.2 mm (cell number/maximum cell size), 27.40 million/1.0 mm, 40.02 million/0.9 mm, 49.22 million/0.8 mm, and 55.98 million/0.8 mm. In all the mesh sets, the cell size near the fuel portholes is refined to 50–75 μm, which is comparable to the Kolmogorov scale of 50 μm estimated based on the fuel inlet properties. As seen in Fig. 5a, the static pressure variations on the lateral wall for all the mesh sets are small and can be considered as almost identical along the whole flow path. For transverse jet flames, the jet penetration may have an important impact on the overall jet mixing and then pressure rise. Thus, the local refined regions near the fuel portholes are enlarged in the mesh with 49.22 million cells to attain the finest mesh with 55.98 million cells. From the comparison, it seems that the pressure profile is insensitive to the local refinement and the additional refinement has been enough. To better quantify the discrepancies, a global relative error is calculated as the summation of the normalized absolute deviations from the finest result, $\sum |p - p_{55.98}|/p_{55.98}$. Figure 5b shows the variation of the global relative error with the characteristic mesh size defined conveniently as $N^{-1/3}$ with N the cell number. As the mesh is refined, the relative error between those predicted by the finest mesh (55.98 million cells) and the coarser meshes decreases gradually from 1.15%, 1.05%, 0.57% to 0.20% for $\Phi = 0.6$, and from 1.24%, 0.84%, 0.38% to 0.30% for $\Phi = 1.0$. The relative error diminishes gradually, showing
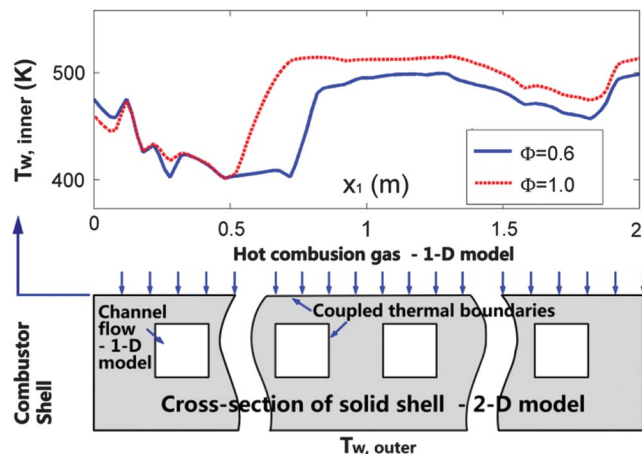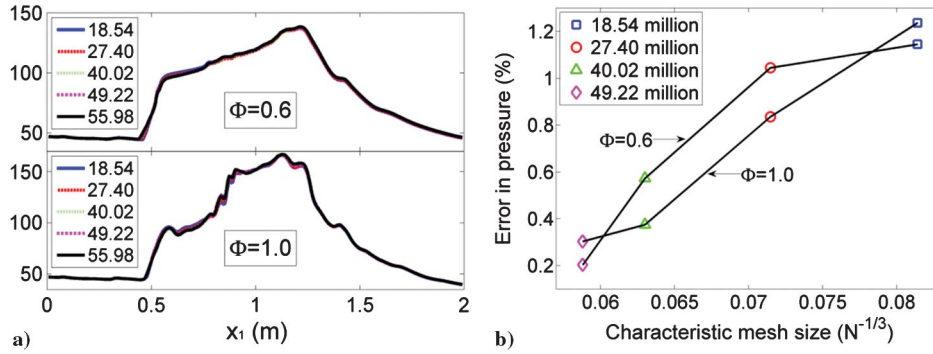
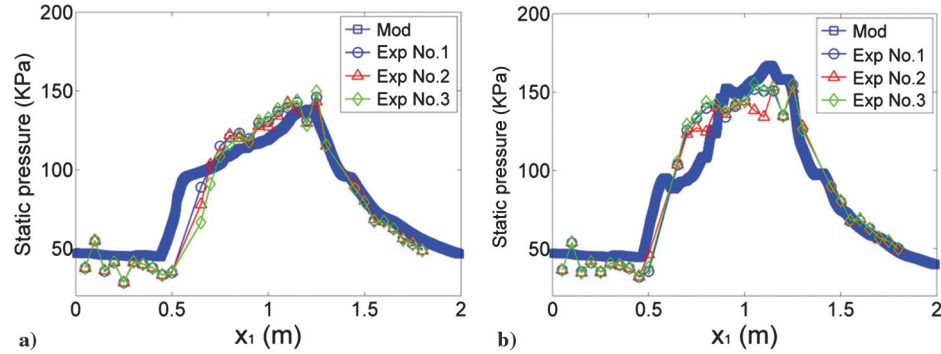**Fig. 5 a) Time-averaged static pressure profiles, and b) relative errors.**

Fig. 6 Time-averaged static pressure profiles for a) $\Phi = 0.6$ and b) 1.0.
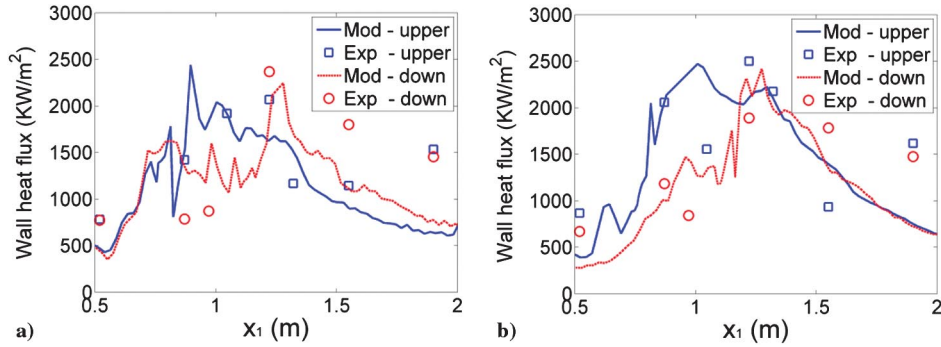

Fig. 7 Time-averaged wall heat flux profiles for a) $\Phi = 0.6$ and b) 1.0.

an asymptotic convergence trend. In consideration of the large unsteadiness in the supersonic reacting flows with moving wave structures, even the maximum relative error of 1.24% is acceptable. All the presented predictions are satisfactory for their almost identical overall profiles. To better capture those delicate instantaneous flow structures as well as to weaken the role of unsophisticated turbulence-related models for supersonic flows, the results of the finest mesh are used in the following analysis.

Figures 6 and 7 compare the time-averaged static pressure on the lateral wall and the time-averaged heat flux on the upper and lower walls with the measurements. The predicted pressure profiles agree well in both the initial pressure rise location and the pressure rise ratio (the ratio of peak to initial pressures) with the three repeated measurements. There is still slight discrepancy on the rising side of the pressure profiles, whereas the pressure profiles agree better on the falling side. The wall heat flux is calculated using Eq. (16). Wall heat flux prediction is influenced not only by the internal combustion modeling but also by the near-wall boundary-layer modeling, and thus it is usually even difficult to accurately predict its order of magnitude. In this study, the peak wall heat flux is around $2\ \mathrm{MW}/\mathrm{m}^2$, which is in accordance with the predictions. The predicted heat flux is comparable with the measurements, at least in the same order of magnitude. The heat flux increases with the inlet temperature and the

mass flow rate [29]; however, the influence of Φ seems to be nonmonotonic and unobvious. The large streamwise variation of the wall heat flux also suggests that a denser spatial sampling should be laid to avoid any potential local overheating.

Figure 8 shows the time-averaged Ma contours for $\Phi = 0.6$ and 1.0, with the sonic line ($Ma = 1$) delimiting the supersonic and subsonic regions. In the following, all the two-dimensional contours are extracted on the streamwise plane through the fuel injector close to the middle plane. The supersonic regions, especially those between the two cavities shrink with the increasing of Φ. This is in expectation because the heat addition becomes higher at $\Phi = 1.0$,
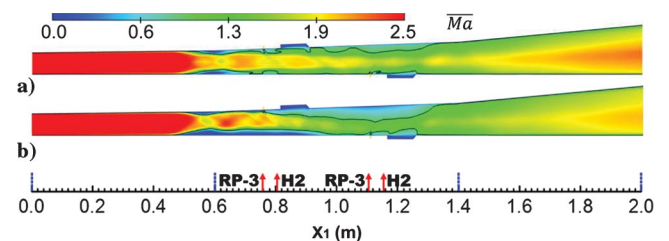

Fig. 8 Time-averaged Ma contours for a) $\Phi = 0.6$ and b) 1.0.

and the heating always drives Ma toward 1 and thermal choking ($dMa/Ma \sim dT_t/T_t$, where T_t is total temperature). A special phenomenon of asymmetric boundary-layer separation was observed for $\Phi = 1.0$. Before the upstream fuel injection, the subsonic regions on the upper and lower sides are roughly in equivalent size for $\Phi = 0.6$, whereas the subsonic region on the lower side is obviously in larger size for $\Phi = 1.0$. It seems that the upstream propagation of the back pressure through the lower boundary layer at $\Phi = 1.0$ "bends" the supersonic core toward the upper wall, which further erodes the subsonic region there. The asymmetric boundary-layer separation causes that the shock wave initiates farther upstream on the lower wall than on the upper wall. The initial shock wave foot is thus tilted with the transverse direction on the lateral wall. The pressure profiles in Fig. 6 are sampled on the middle line of the lateral wall, and thereby the location of initial pressure rise seems to be farther downstream for the higher Φ. Asymmetric boundary-layer separation has also been frequently observed in the experiments, and it further complicates the combustor design. The causes, influencing factors, and suppression methods for asymmetric boundary-layer separation merits future in-depth studies.

The mass-flux-weighted Ma on the cross section perpendicular to the streamwise direction is calculated and then time-averaged:

$$\overline{Ma}_{x_1} = \frac{1}{n} \sum_n \frac{\int (\rho \boldsymbol{u} Ma) \cdot \mathrm{d}\boldsymbol{A}}{\int (\rho \boldsymbol{u}) \cdot \mathrm{d}\boldsymbol{A}} \tag{17}$$

where n is the number of time sequences; the subscript x_1 denotes the streamwise location; ρ and $\boldsymbol{u}$ are, respectively, the flow density and velocity; and A is the cross-sectional area. Figure 9a confirms that as Φ increases, $\overline{Ma}_{x_1}$ becomes lower, except before $x_1 = 0.6$ m, which indicates that the initial oblique shock waves are stronger for $\Phi = 0.6$. From Fig. 8, the upper boundary layer at the initial shock impinging point obviously has a severe separation for $\Phi = 0.6$ than for $\Phi = 1.0$, and then the flow Ma through the narrower aerodynamic throat is adapted to a lower value to accommodate the same mass flow rate. Usually, it is expected that the initial shock train is stronger at higher Φ because the back pressure is higher; however, this study shows that the supersonic flow in a realistic combustor is complex. For example, asymmetric boundary-layer separation may occur. Figure 9b shows the time-averaged ratio of mass flux in supersonic

$$\eta_{Ma} = \frac{1}{n} \sum_n \frac{\int (\rho \boldsymbol{u})_{\overline{Ma} \geq 1} \cdot \mathrm{d}\boldsymbol{A}}{\int (\rho \boldsymbol{u}) \cdot \mathrm{d}\boldsymbol{A}} \tag{18}$$

The supersonic flux ratio decreases significantly as Φ increases, which is in accordance with the shrinkage of supersonic regions in Fig. 8. Although part of the cross-sectional Ma is lower than one and the instantaneous supersonic core seems to be intermittent for $\Phi = 1.0$, the time-averaged supersonic flux ratio is larger than 34% over the whole flow path, indicating that the combustor runs actually in scramjet mode for both cases.

Figure 10 shows the main flow and turbulent structures represented by the second spatial derivative of the density field ($\nabla^2 \rho$) under
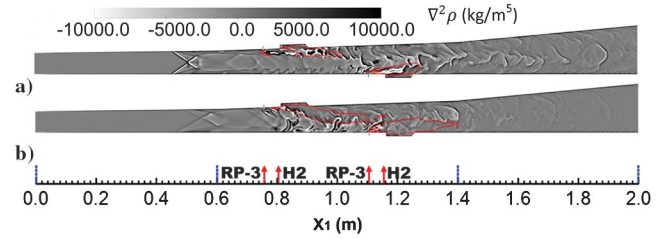
Fig. 10 Instantaneous synthetic shadowgraphs for a) $\Phi = 0.6$ and b) 1.0 with the $\overline{dQ} = 1$ W contours.

different Φs. These synthetic shadowgraphs clearly show the shock waves, fuel stream, and hot combustion layer, that is, those flow structures with a large density gradient. The larger contrast confirms that the initial shock waves are stronger for $\Phi = 0.6$. Weaker reflected shock waves of the initial shock waves impinge on the bow shock wave in front of the fuel jet for $\Phi = 0.6$, and a second reflected shock wave is observed for $\Phi = 1.0$. The fuel-rich mixing layer is more heavily corrugated by the intense heat release as Φ increases. The mean heat release regions enclosed by the $\overline{dQ} = 1$ W contours distribute mainly in the corrugated mixing layer above the cavity and penetrate deeper into the supersonic core as Φ increases. From the initial flame anchoring locations, the flame stabilizes in cavity mode for the upstream fuel jet, but in the jet-wake mode for the downstream fuel jet. At least part of the reaction zones overlap with the supersonic region, where the compressibility effect on the subgrid-scale combustion should be taken into account in the future study.

The streamwise mixing and combustion efficiencies and total pressure loss for the combustors under different Φs are compared in Fig. 11. The time-averaged mixing efficiency is calculated as

$$\eta_{\text{mix}} = \frac{1}{n} \sum_n \frac{\dot{m}_{\text{fuel,mixed}}}{\dot{m}_{\text{fuel,total}}} = \frac{1}{n} \sum_n \frac{\int (\rho \boldsymbol{u} Y_{f,\text{react}}) \cdot \mathrm{d}\boldsymbol{A}}{\int (\rho \boldsymbol{u} Y_f) \cdot \mathrm{d}\boldsymbol{A}} \tag{19}$$

with

$$Y_{f,\text{react}} = \begin{cases} Y_f & Y \leq Y_{f,\text{st}} \\ Y_{f,\text{st}} \dfrac{1 - Y_f}{1 - Y_{f,\text{st}}} & Y > Y_{f,\text{st}} \end{cases}$$

where $\dot{m}_{\text{fuel,mixed}}$ and $\dot{m}_{\text{fuel,total}}$ are the mass flow rates of mixed and total fuel, Y_f is the fuel mass fraction, $Y_{f,\text{react}}$ is the mass fraction of the fuel that can be reacted, and $Y_{f,\text{st}}$ is the fuel mass fraction at stoichiometric condition. Combustion efficiency is calculated as the ratio of the fuel that has been completely converted to the final stable products (e.g., CO_2 and H_2O). Because of the existence of H_2O in the incoming vitiated air, the definition of combustion efficiency based on H_2O for hydrogen combustion [30] is reformed to be based on CO_2 for hydrocarbon fuels
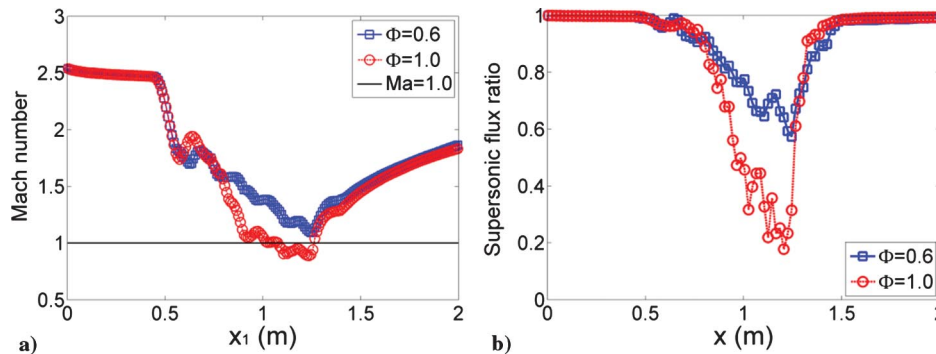
Fig. 9 Time-averaged and mass-flux-weighted spatial-averaged a) Ma and b) supersonic flux ratio.
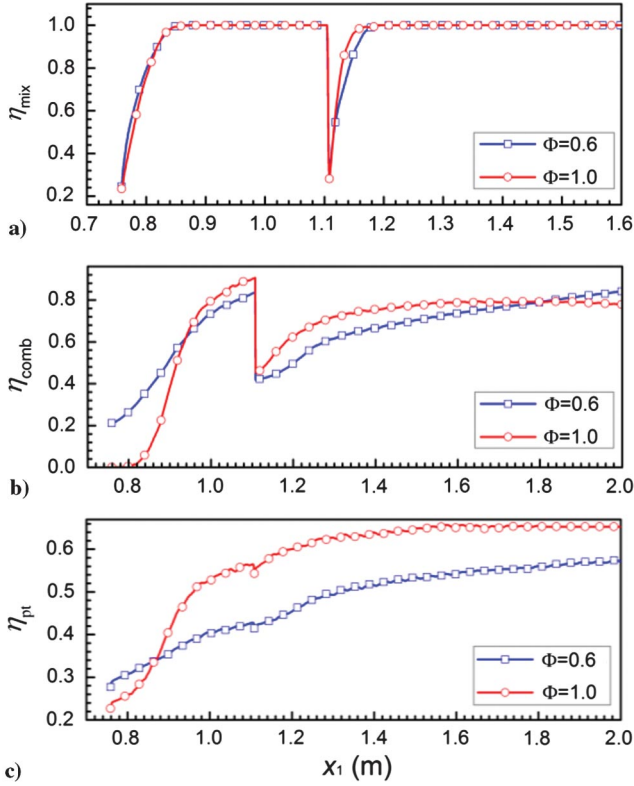
Fig. 11   Time-averaged a) mixing efficiency, b) combustion efficiency, and c) total pressure loss.

$$\eta_{\text{comb}} = \frac{1}{n} \sum_n \frac{[(1/\nu_{CO_2}) \int (\rho \boldsymbol{u} Y_{CO_2}) \cdot d\boldsymbol{A} / W_{CO_2}]^{x_1}_{\text{inlet}}}{\dot{m}_{\text{fuel,total}} / W_{\text{fuel}}} \tag{20}$$

where the subscript "inlet" denotes variables on the inlet plane, the superscript "x_1" denotes the current streamwise location, the area integration is conducted on each cross sections at different streamwise locations, Y_{CO_2} is the mass fraction of CO_2, W is the molecular weight of the fuel or CO_2 denoted by the subscript, and ν_{CO_2} is the stoichiometric coefficient of CO_2. The total pressure loss is defined as

$$\eta_{P_t} = 1 - \frac{1}{n} \sum_n \frac{\int (\rho \boldsymbol{u} P_{t,x_1}) \cdot d\boldsymbol{A}}{\int (\rho \boldsymbol{u} P_{t,\text{inlet}}) \cdot d\boldsymbol{A}} \tag{21}$$

where P_{t,x_1} and $P_{t,\text{inlet}}$ are the total pressure at the streamwise location x_1 and the inlet plane, respectively.

From Fig. 11a, it can be seen that the fuel mixing distances are generally short and all mixing completes within a moving distance of 8 cm. Note that the mixing efficiency does not start from zero at the fuel injection location because part of fuel has been entrained and convected slightly upstream by the recirculating flows in the separated boundary layer. The mixing efficiencies are almost identical for the two cases. In comparison with the case at $\Phi = 1.0$, the mixing at $\Phi = 0.6$ is slightly faster in the upstream fuel jet and slower in the downstream fuel jet. Both the mixing differences can be explained from the flow residence time: 1) the boundary layer has been considerably thickened before the upstream fuel jet at $\Phi = 0.6$ than at $\Phi = 1.0$ to provide a low-speed flow bay for the fuel mixing; 2) the flow Ma has been significantly reduced, to even subsonic around the downstream fuel jet for $\Phi = 1.0$, and thus the flow residence time there is longer. And also the richer eddies at $\Phi = 1.0$ introduced by the upstream jet-crossflow interaction help to improve the downstream mixing.

Although the mixing is generally quick and complete, the combustion efficiencies in Fig. 11b vary from case to case, because the reaction progress is also influenced by local flow conditions. The

reactions even start before the upstream fuel injection location for $\Phi = 0.6$, while basically no reaction for $\Phi = 1.0$ although part of fuel has been mixed there. In the initial mixing region before $x_1 = 0.95$ m, the combustion efficiency at $\Phi = 0.6$ is obviously higher than $\Phi = 1.0$. The reason can be that the large subsonic region before the upstream fuel jet at $\Phi = 0.6$ provides an ideal reaction bay with higher temperature yet low flow speed, whereas the subsonic region at the same location for $\Phi = 1.0$ has been heavily eroded by the supersonic core. Since $x_1 = 0.95$ m, the combustion efficiency of $\Phi = 1.0$ exceeds that of $\Phi = 0.6$, because both the pressure and temperature are higher while the flow speed is overall lower for $\Phi = 1.0$. One interesting observation is that the final combustion efficiency at the expander outlet rises again to a higher value of 84% for $\Phi = 0.6$ than the value of 78% for $\Phi = 1.0$. This is possibly because the oxygen is overall richer to allow a more complete conversion of the fuel into stable products (e.g., CO_2 and H_2O), while plenty of incomplete products (e.g., CO) still exist till the end of the expander for $\Phi = 1.0$ as observed from the modeling results.

Corresponding to the earlier initial reactions at $\Phi = 0.6$, the total pressure loss shown in Fig. 11c is higher before $x_1 = 0.95$ m. After $x_1 = 0.95$ m, the total pressure loss for $\Phi = 1.0$ is in average 23% and in maximum 36% higher than that for $\Phi = 0.6$. This is because the heat release rate is higher for $\Phi = 1.0$ and correspondingly the Rayleigh heating loss causes a larger total pressure loss. The final total pressure losses approach the steady values of 57% and 65% at the combustor exit for $\Phi = 0.6$ and 1.0, respectively.

Figure 12 shows the distributions of Takeno Flame Index (TFI) [31] and heat release rate at the same instantaneous time in the burner section for $\Phi = 1.0$. TFI [31] denotes the premixed and the non-premixed flame modes with positive and negative values, respectively. The upstream combustion region is in non-premixed flame mode from the fuel porthole to the upwind side of the mixing layer, and the premixed flame mode exists mainly in a thin layer on the leeward side of the mixing layer and anchored at the leading edge of the upstream cavity. The downstream combustion region is composed of the non-premixed mode in the fuel jet core and the premixed mode in the surrounded jet wake. The premixed regions are helpful to stabilize the flame through acting as an igniter for the neighbor non-premixed regions [32]. In addition to the positive heat
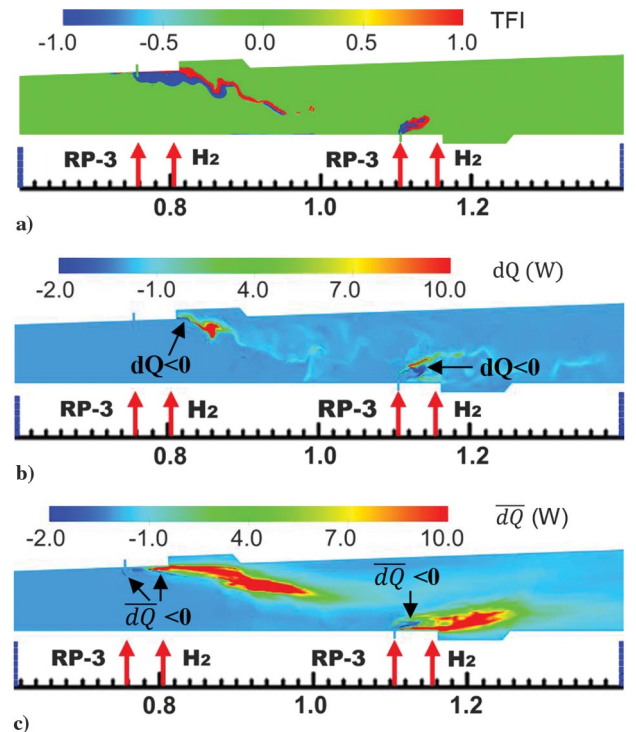
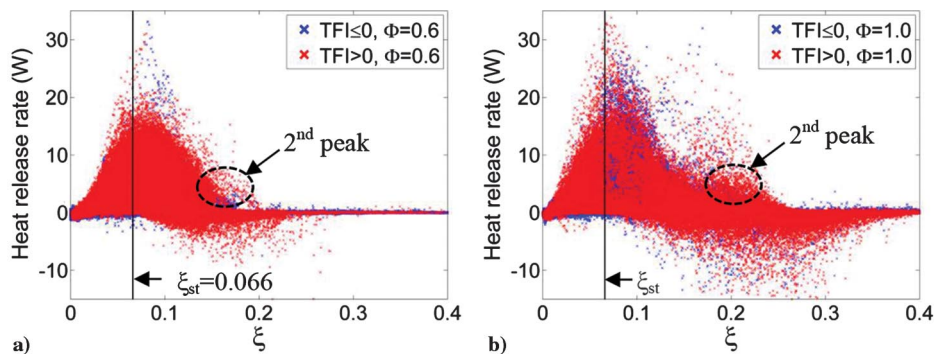**Fig. 12   Instantaneous a) TFI and b) heat release rate, and c) time-averaged heat release rate for $\Phi = 1.0$.**

Fig. 13 Historic statistic of heat release rate versus mixture fraction for a) $\Phi = 0.6$ and b) 1.0.

release rate, negative heat release rate can also be observed, for example, near the leading edge of the upstream cavity and in the jet wake of the downstream fuel jet. Those negative values correspond to the endothermic pyrolysis reactions from large-molecule hydrocarbons to small-molecule ones (e.g., C_3H_6, C_2H_4). The mean heat release rate clearly indicates that those pyrolysis reactions most frequently occur in the upwind side of the fuel jet immediately after the fuel injection, in the frontal edge of the upstream combustion region, and in the downstream jet wake. The common properties in those regions are fuel-rich ($\xi > \xi_{st}$) and bearing high temperature ($T > 1500$ K) due to aerodynamic heating or upstream preheating. The distribution of mean heat release rate is significantly different from that of instantaneous one, indicating that the reaction regions are in large unsteadiness. The mean heat release rate distribution clearly shows that the flame stabilization is in cavity mode for the upstream combustion but jet-wake mode for the downstream combustion. All the combustion reactions take place in the mixing layer above the cavity with trivial reactions inside the cavity.

The distributions of heat release rate in the mixture fraction space are compared for the two Φs in Fig. 13. As seen, there is generally little pyrolysis reactions in the oxygen-rich side, and most of the pyrolysis reactions occur in the range of $[\xi_{st}(= 0.066), 0.28]$ for $\Phi = 0.6$ and $[\xi_{st}, 0.38]$ for $\Phi = 1.0$. The lowest negative values corresponding to the most violent pyrolysis reactions occur at around $\xi = 0.18$ for $\Phi = 0.6$ and $\xi = 0.25$ for $\Phi = 1.0$. The pyrolysis region shifts toward fuel richer conditions under higher Φ, probably because the jet core with a higher jet momentum penetrates deeper and thereby has a better contact with the high-stagnation-temperature incoming flow. The premixed (TFI > 0) and non-premixed (TFI $\leq$ 0) points are marked with different colors in Fig. 13. However, it is hard to distinguish the premixed and non-premixed regions in the $dQ - \xi$ space; therefore, it is said that the combustion is composed of an ensemble of premixed, diffusion, and partially premixed flames as well. For $\Phi = 0.6$, 40% of exothermic reactions (defined as $dQ > 1$ W) occur under premixed mode, whereas 91% of endothermic reactions (defined as $dQ < -1$ W) occur under non-premixed mode. For $\Phi = 1.0$, 26% of exothermic reactions occur under premixed mode, while 76% of endothermic reactions occur under non-premixed mode. It seems that most of the endothermic reactions occur under the premixed mode and the ratio of premixed mode decreases with the increasing of Φ. Under oxygen-rich conditions, the large-molecule hydrocarbons may either react with the O atom and the OH radical, or undergo reaction with the H atoms, producing C_1, C_2, and C_3 fragments. Those CC bond-breaking reactions are usually endothermic, and thus a very small percentage of negative heat release under fuel-lean combustion can be observed in Fig. 13. But the overall heat release is positive because the subsequent exothermic oxidations of those C_1, C_2, and C_3 fragments become dominant. The positive values correspond to the exothermic oxidation reactions, with the peak values occur slightly shifting to the fuel-rich side. Such rich shifting is believed to be caused by the reduced heat release due to product dissociations [33], for example, the dissociation of H_2O and CO_2 into H_2, O_2, and CO, which is in smaller extent on the rich side than on the lean side. In addition to the large peak around ξ_{st}, a secondary smaller peak in the fuel-rich side

can be observed, especially clearly for the higher Φ. The secondary peak most likely corresponds to the initial oxidation chain reactions of small-molecule hydrocarbons (e.g., PC_4H_9, C_3H_6, and C_2H_5) with OH, O, O_2, and so on, which form even smaller-molecule hydrocarbons such as C_2H_3, CH_3, and CH_2O. The pyrolysis and oxidation reactions are both intensified from the fuel-lean case to the stoichiometric case, as indicated by the variation range of heat release rate, which is -10 to 30 W for $\Phi = 0.6$, while -15 to 35 W for $\Phi = 1.0$.

B. Vorticity and Its Evolution Mechanisms

The contour of vorticity magnitude in Fig. 14a shows that the boundary layer and flow around the fuel portholes have relatively large values and are thus tend to produce more vortices. The fuel flow in the injection tubes is quite uniform with weak vorticity generated there, but strong vorticity is generated immediately outside the portholes. The vortices are represented by 3-D isosurfaces of λ_2 (the second eigenvalue of the velocity gradient tensor) colored by static temperature and underlain by numerical shadowgraph. Because of the leading edge of the upstream cavity, the internal flow is fully filled with streak-like vorticity and the corresponding large-scale coherent structures (Fig. 14b), which are mainly caused by the distortions of intense heat release and transverse injection momentum. The vorticity weakens and vortices thin obviously in the expander. Because the fuel jet cannot persist long under the reacting condition, the vortex types commonly recognized in nonreacting jets in supersonic crossflow (JISCs), for example, the counterrotating vortex pair and Ω vortices [34], are unobvious in Fig. 14b.

Streamwise distributions of mean vorticity magnitude calculated as

$$|\mathbf{\Omega}|_{x_1} = \frac{1}{n}\sum_n \frac{\int(\rho \mathbf{u}|\mathbf{\Omega}|)\cdot \mathrm{d}\mathbf{A}}{\int(\rho \mathbf{u})\cdot \mathrm{d}\mathbf{A}} \qquad (22)$$

for the two Φs on the cross sections perpendicular to the streamwise direction are plotted in Fig. 15a. The three peaks subsequently correspond to the boundary-layer separation point impinged by the initial oblique shock waves, the locations slightly before the upstream and downstream fuel injectors. Because the shock train moves slightly downstream and the recirculation region before the upstream fuel jet is narrower, the first and second peaks occur at farther downstream locations for $\Phi = 1.0$. There is initial vorticity for the inflow due to shear stress in the near-wall layer. Both the vorticities at $\Phi = 0.6$ and
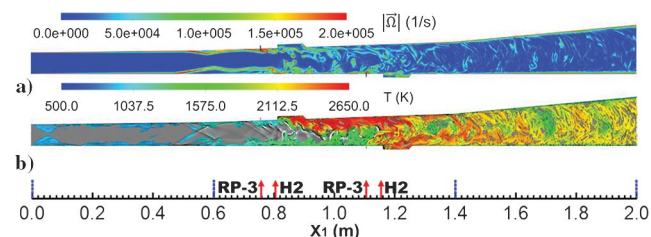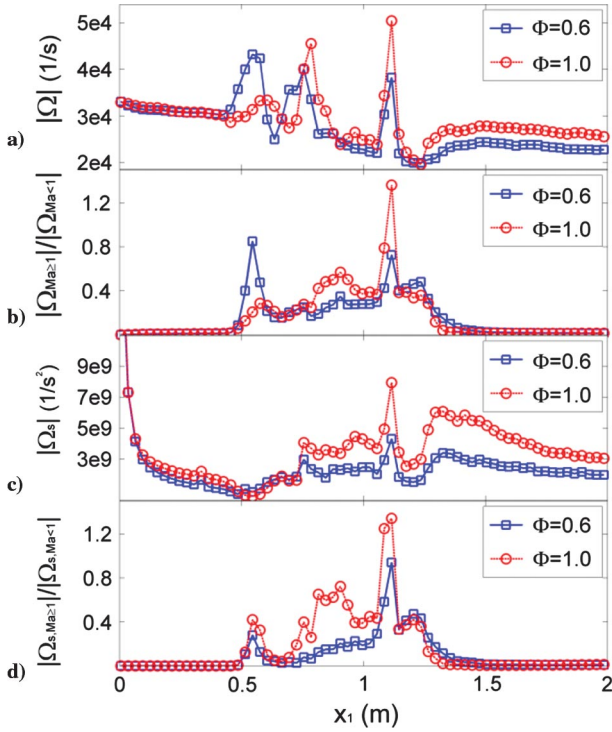

Fig. 14 Instantaneous a) vorticity magnitude $|\mathbf{\Omega}|$ and b) vortex structures for $\Phi = 1.0$.

Fig. 15 Time-averaged and mass-flux-weighted spatial-averaged a) vorticity magnitude, b) supersonic-to-subsonic vorticity ratio, c) total vorticity source-term magnitude, and d) supersonic-to-subsonic ratio of total vorticity source term.

1.0 reach their minimum values at the streamwise location near the trailing edge of the downstream cavity. Then the vorticities recover in a short distance by roughly 40% and 26% for $\Phi = 0.6$ and 1.0 at the entrance interface of the expander, and decay steadily toward the end of the expander. The ratios between the mean vorticity in supersonic and subsonic regions are shown in Fig. 15b. As seen, from the initial shock wave location roughly at $x_1 = 0.5$ m to the end the burner section, the supersonic and subsonic mean vorticities are in the same order of magnitude, and the supersonic mean is lower than the subsonic mean except at several individual locations. In the remaining locations, the supersonic mean is far smaller than the subsonic one for two orders of magnitude. This indicates that the subsonic regions are responsible for the main vortex generation. The vorticity and the supersonic-subsonic vorticity ratio are both overall slightly higher for $\Phi = 1.0$, except at the initial shock impinging point where both the vorticity and the ratio are higher for $\Phi = 0.6$. This is because the initial oblique shock waves are stronger at $\Phi = 0.6$, as confirmed by the lower postshock Ma in Figs. 8 and 9a, and therefore more intense vorticity is produced by a larger entropy gradient after the shock waves according to the Crocco's theorem.

Vorticity analysis is an important step to identify the mixing mechanism and find strategies for mixing enhancement because the turbulent vortices are responsible for most of the macromixing. The vorticity evolution is governed by the compressible vorticity transport equation:

$$\frac{\partial \mathbf{\Omega}}{\partial t} = \underbrace{-(\mathbf{u}\cdot\nabla)\mathbf{\Omega}}_{\mathbf{\Omega}_{s,\text{conv}}} \underbrace{-\mathbf{\Omega}(\nabla\cdot\mathbf{u})}_{\mathbf{\Omega}_{s,\text{dila}}} + \underbrace{(\mathbf{\Omega}\cdot\nabla)\mathbf{u}}_{\mathbf{\Omega}_{s,\text{VS}}} + \underbrace{\nu\nabla^2\mathbf{\Omega}}_{\mathbf{\Omega}_{s,\text{diff}}} \underbrace{(\nabla p \times \nabla\rho)/\rho^2}_{\mathbf{\Omega}_{s,\text{Baro}}}$$
$$\underbrace{\qquad\qquad\qquad\qquad\qquad\qquad}_{\mathbf{\Omega}_{s,t}}$$

$$(23)$$

As seen, five main physical mechanisms contribute to the vorticity evolution through terms denoted as $\mathbf{\Omega}_{s,\text{conv}}$ for the convective term, $\mathbf{\Omega}_{s,\text{dila}}$ for the dilatational term, $\mathbf{\Omega}_{s,\text{VS}}$ for the vortex stretching term, $\mathbf{\Omega}_{s,\text{diff}}$ for the diffusion term, and $\mathbf{\Omega}_{s,\text{Baro}}$ for the baroclinic term. The five terms are summed as $\mathbf{\Omega}_{s,t}$. As an approximation, the resolved values from the IDDES modelings are used to estimate those source

terms. To quantify their orders of magnitude, time-averaged integrations on the cross section at each streamwise location are calculated as

$$|\mathbf{\Omega}_s|_{x_1} = \frac{1}{n}\sum_n \frac{\int(\rho\mathbf{u}|\mathbf{\Omega}_s|)\cdot d\mathbf{A}}{\int(\rho\mathbf{u})\cdot d\mathbf{A}} \qquad (24)$$

where $\mathbf{\Omega}_s$ represents the different source term in the RHS of Eq. (23). The mean magnitudes of total source term $|\mathbf{\Omega}_{s,t}|_{x_1}$ for the two Φs are shown in Fig. 15c on the same axes with the mean vorticity magnitudes. One obvious observation is that $|\mathbf{\Omega}_{s,t}|_{x_1}$ is higher for the higher Φ, since the distortions by the transverse jet and heat release rate are heavier. Because the upstream fuel injection at $x_1 = 0.7585$ m, $|\mathbf{\Omega}_{s,t}|_{x_1}$ almost doubles for $\Phi = 1.0$ than for $\Phi = 0.6$. The supersonic-to-subsonic ratios of total vorticity source-term shown in Fig. 15d are comparable for the two Φs from the initial oblique shock waves to the end of the burner section, with the one at $\Phi = 1.0$ slightly higher. The supersonic-to-subsonic ratios are around 1% in the expander and almost zero in the isolator before the initial shock waves.

The contours of individual vorticity source terms at the same instantaneous time are shown in Fig. 16. $\mathbf{\Omega}_{s,\text{conv}}$ is responsible for the convection transport of vorticity along with the flow, and thus it has higher magnitude in the high-speed core flow than near the wall. $\mathbf{\Omega}_{s,\text{dila}}$ is important in supersonic reacting flows, where the volume expansion due to heat release will decrease the vorticity magnitude, but the compression by shock waves will reversely increases vorticity and enhances mixing [35]. In the sense of the conservation of angular momentum principle, $\mathbf{\Omega}_{s,\text{dila}}$ does not create or destroy any vortices, but only redistributes its vorticity through diluting or concentrating without changing the vorticity direction. As seen, $\mathbf{\Omega}_{s,\text{dila}}$ is higher around the underexpanded fuel jets, across the sonic interfaces and in the reacting layers, that is, those regions where the flow has been severely compressed or expanded. $\mathbf{\Omega}_{s,\text{VS}}$ is an important term responsible for the generation of smaller vortices and the energy cascade in turbulence dynamics. It enhances vorticity through stretching the vortex tubes into smaller yet longer ones, mainly in the streamwise direction. Thus, a nonzero value of $\mathbf{\Omega}_{s,\text{VS}}$ denotes the existence of true vortices, while the vorticity denotes the potentiality of forming vortices. For this reason, $|\mathbf{\Omega}_{s,\text{VS}}|$ usually has higher values in the flows enriched by vortices, for example, around the fuel jet, in the fuel shear/mixing layer and the sonic shear layer between the supersonic core flow and the outward subsonic regions, and inside the cavity. When one vortex has been stretched to be long, the vortex tube becomes prone to be separated from its maternal vortex, and such a vortex break-up process is the main mechanism to transfer turbulent energy into smaller-scale vortices. Thereby, the higher magnitude of $\mathbf{\Omega}_{s,\text{VS}}$ generally corresponds to the flow regions with rich smaller vortices and its start corresponds to where large-scale vortices start to break up into smaller ones. The nondimensional analysis $\mathbf{\Omega}_{s,\text{diff}} \sim Re^{-1}\nabla^2\mathbf{\Omega}$ indicates that $\mathbf{\Omega}_{s,\text{diff}}$ is generally weak in high-Re supersonic flows. In addition to the similar distribution of higher values with $|\mathbf{\Omega}_{s,\text{VS}}|$, $\mathbf{\Omega}_{s,\text{diff}}$ has extremely high value in the boundary layer. Specifically, $\mathbf{\Omega}_{s,\text{diff}}$ has an effect of transferring vorticity from the wall into the core flow, and then diffuse it [35]. Using the inlet properties of the fuel jet to nondimensionalize the baroclinic term, the magnitude of $\mathbf{\Omega}_{s,\text{Baro}}$ is in proportion to $(P_t/\rho_t)f_1(Ma) \sim (T/W_f)f_2(Ma)$, where ρ_t is the density at stagnation condition, W_f is the molecular weight of the fuel, and f_1 and f_1 are monotone-increasing functions of Ma. From the proportional relation, two inferences can be drawn: 1) $\mathbf{\Omega}_{s,\text{Baro}}$ may be negligible in subsonic frozen-chemistry flows with low T and Ma, but should weightily contributes to the mixing in supersonic reacting flows [35], and 2) heavier-molecule fuels like kerosene will suppress its influence on the vorticity generation. The shown magnitude of $\mathbf{\Omega}_{s,\text{Baro}}$ has two obvious peaks, one in the immediately issued jets where rapid expansion and strong shock structures are present, and the other in the reacting shear layer where the lower-density flow side is driven faster by the pressure gradient tangent to
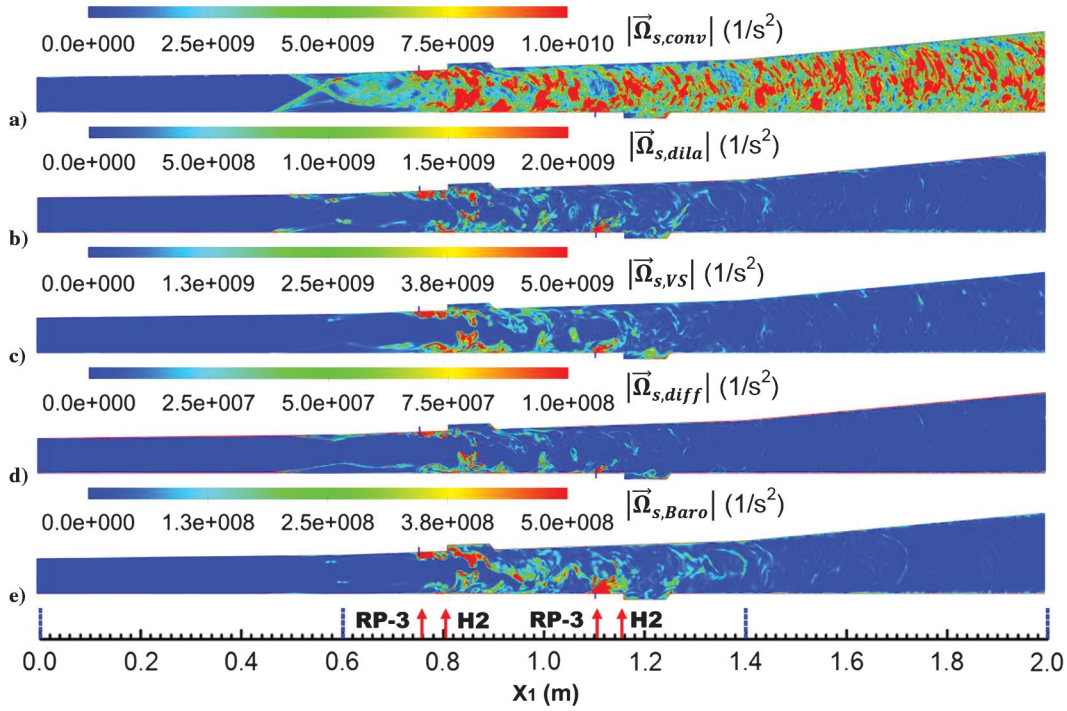
Fig. 16   Magnitudes of a) $\Omega_{s,\text{conv}}$, b) $\Omega_{s,\text{dila}}$, c) $\Omega_{s,\text{VS}}$, d) $\Omega_{s,\text{diff}}$, and e) $\Omega_{s,\text{Baro}}$ for $\Phi = 1.0$.

the layer interface and thus vorticity generates. The baroclinic torque is an important physical mechanism extensively used in the design of passive mixing enhancers, for example, pylons, struts, and ramps [36].

The streamwise variations of the time-averaged individual source-term magnitudes calculated similarly with Eq. (24) are shown in Fig. 17 for the main vortex generation regions from the burner inlet to the expander exit. At $\Phi = 0.6$, the streamwisely averaged values from $x_1 = 0.6$ to 2.0 are 2.62×10^9 s^{-2} for $|\Omega_{s,\text{conv}}|$, 9.43×10^8 s^{-2} for $|\Omega_{s,\text{dila}}|$, 1.41×10^8 s^{-2} for $|\Omega_{s,\text{VS}}|$, 1.04×10^8 s^{-2} for $|\Omega_{s,\text{diff}}|$, and 4.22×10^7 s^{-2} for $|\Omega_{s,\text{Baro}}|$. At $\Phi = 1.0$, the streamwisely averaged values from $x_1 = 0.6$ to 2.0 are 4.52×10^9 s^{-2} for $|\Omega_{s,\text{conv}}|$, 1.77×10^9 s^{-2} for $|\Omega_{s,\text{dila}}|$, 2.05×10^8 s^{-2} for $|\Omega_{s,\text{VS}}|$, 1.36×10^8 s^{-2} for $|\Omega_{s,\text{diff}}|$, and 5.69×10^7 s^{-2} for $|\Omega_{s,\text{Baro}}|$. As seen, $|\Omega_{s,\text{conv}}|$ and $|\Omega_{s,\text{dila}}|$ have the highest order of magnitude of $\sim O(10^9)$ s^{-2}, $|\Omega_{s,\text{VS}}|$ and $|\Omega_{s,\text{diff}}|$ have the medium order of magnitude of $\sim O(10^8)$ s^{-2}, whereas $|\Omega_{s,\text{Baro}}|$ has the lowest order of magnitude of $\sim O(10^7)$ s^{-2}. This is slightly different from the observation for supersonic hydrogen combustion in [35], where $|\Omega_{s,\text{dila}}|$, $|\Omega_{s,\text{VS}}|$, and $|\Omega_{s,\text{Baro}}|$ have the same order of magnitude. From the comparison, all the individual vorticity source terms increase at the higher Φ.

From Figs. 17a and 17b, the source terms are obviously overall higher at $\Phi = 1.0$ for $|\Omega_{s,\text{conv}}|$ and $|\Omega_{s,\text{dila}}|$, while generally comparable for the others. $|\Omega_{s,\text{conv}}|$ are generally identical before the upstream fuel injection for the two Φs and almost doubles for $\Phi = 1.0$ after the upstream fuel injection. $|\Omega_{s,\text{dila}}|$ is generally identical before the trailing edge of the upstream cavity at $x_1 = 0.9$ m, and roughly doubles for $\Phi = 1.0$ after the trailing edge of the upstream cavity.

From Fig. 17c, $|\Omega_{s,\text{VS}}|$ is 90% higher between the upstream and downstream fuel injections for $\Phi = 1.0$, which is the main region for the break-up of large-scale vortices into smaller ones, and is comparable with the low Φ value in the remaining locations. Two peaks corresponding to the fuel injections are identified. This indicates that the vortex stretching is sensitively influenced by the jet-crossflow interactions.

From Fig. 17d, $|\Omega_{s,\text{diff}}|$ is overall smaller before $x_1 = 1.04$ m for $\Phi = 1.0$, but becomes apparently higher after $x_1 = 1.04$ m. The vortex distributions show that the small-scale vortices are widely

distributed in the supersonic crossflow before $x_1 = 1.04$ m for $\Phi = 0.6$ but almost absent for $\Phi = 1.0$; the tremendous of large-scale vortices still exist in the expander for $\Phi = 1.0$, whereas the vortex sizes are smaller yet more uniform for $\Phi = 0.6$. Because the diffusive term has a similar effect with the vortex stretching term to diminish the existing vortices, it is not surprising that it is weaker in the front part but stronger in the latter part for $\Phi = 1.0$.
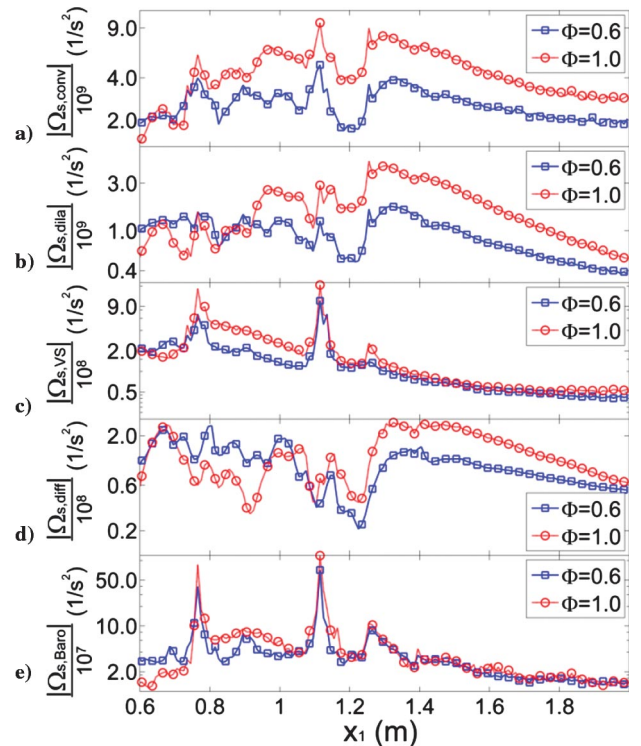

Fig. 17   Time-averaged and mass-flux-weighted spatial-averaged a) $|\Omega_{s,\text{conv}}|$, b) $|\Omega_{s,\text{dila}}|$, c) $|\Omega_{s,\text{VS}}|$, d) $|\Omega_{s,\text{diff}}|$, and e) $|\Omega_{s,\text{Baro}}|$ in logarithmic scale for the vertical axis.
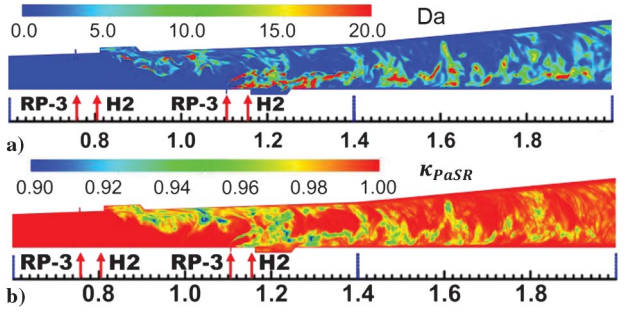
Fig. 18 Instantaneous contours of a) Da and b) $\kappa_{\mathrm{PaSR}} = \tau_c/(\tau_c + \tau_{\mathrm{mix}})$ for $\Phi = 1.0$.

From Fig. 17e, $\Omega_{s,\mathrm{Baro}}$ is larger before the upstream fuel injection for $\Phi = 0.6$ and stronger between the two fuel injections for $\Phi = 1.0$, and almost coincides with each other since the downstream fuel injection. The stronger baroclinic term before the upstream fuel injection for $\Phi = 0.6$ is due to the stronger initial oblique shock waves, and the stronger baroclinic term between the two fuel injections for $\Phi = 0.6$ can be explained by the larger density difference across the reacting layer caused by the more intense heat release rate.

C. Turbulence-Chemistry Interaction and Combustion Modes

Figures 18a and 18b, respectively, show the distributions of Damköhler number (Da) and the coefficient in PaSR model, which are related to turbulence-chemistry interaction (TCI). Da is calculated as the ratio of subgrid turbulent time scale τ_Δ to the chemical time scale τ_c: $Da = \tau_\Delta/\tau_c$, where τ_Δ and τ_c are calculated as the same as those used in the PaSR model. Referring to Fig. 12b, those high-Da regions ($Da > 10$) correspond not only to the main heat release regions but also to the downstream regions with mild heat release rate in the order of ~1 W. This is because the downstream combustion reactions are mainly the active chain reactions converting intermediate products (e.g., CO, H, OH, and H_2O) into the final stable products (CO_2 and H_2O), where the chemical time scales are smaller. The PaSR coefficient, $\kappa_{\mathrm{PaSR}} = \tau_c/(\tau_c + \tau_{\mathrm{mix}})$, is related to the Karlovitz number Ka as $\kappa_{\mathrm{PaSR}} \approx Ka/(1 + Ka)$ assuming $\tau_{\mathrm{mix}} \approx \tau_k$. The Ka can become infinitely large ($Ka \rightarrow \infty$) if the local chemistry is extremely slow, whereas the κ_{PaSR} becomes a unity quantity; thus, it is more convenient to describe the turbulence-chemistry interaction by κ_{PaSR} rather than by Ka. The distribution of low κ_{PaSR} highly resembles the distribution of high Da, that is, in the reacting mixing layer extended from the trailing edge of the upstream cavity to the downstream cavity and in the reacting mixing layer since the downstream jet wake till the end of the expander.

A manipulation of the Borghi's diagram [37] is shown in Fig. 19, where the abscissa of Re (Reynolds number) is replaced by κ_{PaSR}. The distributions of Da both peak at around $\kappa_{\mathrm{PaSR}} = 0.95$. Referring to Fig. 12b, $\kappa_{\mathrm{PaSR}} = 0.95$ corresponds to the downstream regions with

mild heat release rate in the order of ~1 W, where the chain termination reactions are more active; thus, unsurprisingly the chemical time scales are smaller. The fuel-lean case under $\Phi = 0.6$ seems to have more data points with $Da > 1000$, probably because those chain termination reactions converting intermediate products (e.g., CO, H, OH, and H_2O) into the final stable products (CO_2 and H_2O) are more complete under the oxygen-rich condition. The data points span a wider range of κ_{PaSR} from 0.8 to 0.5 for $\Phi = 1.0$. A close examination found that those low-κ_{PaSR} spots in Fig. 18b do not correspond to high heat release rate but always to low turbulent kinetic energy. This suggests that the turbulent mixing and the chemical reactions are not simultaneous, and then a delayed burning after mixing in a downstream weakly turbulent region will produce the relatively low κ_{PaSR}. The main heat release region denoted in Fig. 10 is confined to a narrow layer for $\Phi = 0.6$ but penetrates deeply into the core flow for $\Phi = 0.6$, and thus the spatial mismatch between the mixing and the burning aggravates and the low κ_{PaSR} is more likely to occur under a higher jet momentum.

A statistics of the fraction of data point distribution in each range is listed in Table 2, where from the bottom left corner to the upper right the chemistry slows down and the flame front thickens gradually. A low κ_{PaSR} value below 0.5 (equivalent to $Ka < 1$) implies that kinetics are faster compared with turbulent mixing and $\delta_l < l_k$ (where δ_l is flame thickness and l_k is the dissipative scale). However, as displayed in Figs. 18 and 19 even the lowest κ_{PaSR} is above 0.5 and most of the values are close to 1.0, implying that the flame is at least partially distributed with the smallest eddies entering into the flame and thicken its front ($\delta_l > l_k$). $Da\gg1$ means that kinetics are extremely fast compared with transport, and the assumption of fast chemistry is then be justified. The chemistry is considered as slow for $Da \leq 10$, medium for $10 < Da \leq 100$, fast for $100 < Da \leq 1000$, and extremely fast for $Da > 1000$. The table can be divided into three main zones: slow chemistry zone, with $Da \leq 10$; thin reaction zone, with $Da > 10$ and $\kappa_{\mathrm{PaSR}} \geq 0.5$ ($Ka \geq 1$); and flamelet zone, with $Da > 10$ and $\kappa_{\mathrm{PaSR}} < 0.5$ ($Ka < 1$). From the statistics, most of the data points, 95.03% for $\Phi = 0.6$ and 94.46% for $\Phi = 1.0$, are distributed in the slow chemistry zone, whereas only a small percentage, 4.97% for $\Phi = 0.6$ and 5.54% for $\Phi = 1.0$, are distributed in the thin reaction zone, and nearly zero in the flamelet zone. Thus for the current examined kerosene-fueled scramjet combustor, the modeling of the turbulence-chemistry coupling should be based on a harmonic combustion model, where the reaction rate is controlled by both the micromixing rate and the reaction rate. For hydrogen-fueled scramjet combustors, the chemical time scale is of $\sim O(10^{-3})$ smaller than that of kerosene, and the flamelet mode may exist broadly in the domain, and thereby less computationally expensive flamelet models would be applicable. However, this luxury is not available to the modeling of kerosene-fueled combustors.

Figure 20 shows the mean scalar dissipation rate $\tilde\chi$ in logarithmic scale, which is calculated by its relationship with the mixture fraction variance $\tilde\chi = C_D \tilde\xi''^2/\tau_\Delta$ [38], with $C_D = 4.0$ and the mixture fraction variance given by an algebraic model $\tilde\xi'' = 0.5 d_{\mathrm{IDDES}}^2 |\nabla\tilde\xi|^2$. The mean scalar dissipation rate is in reverse proportion to the
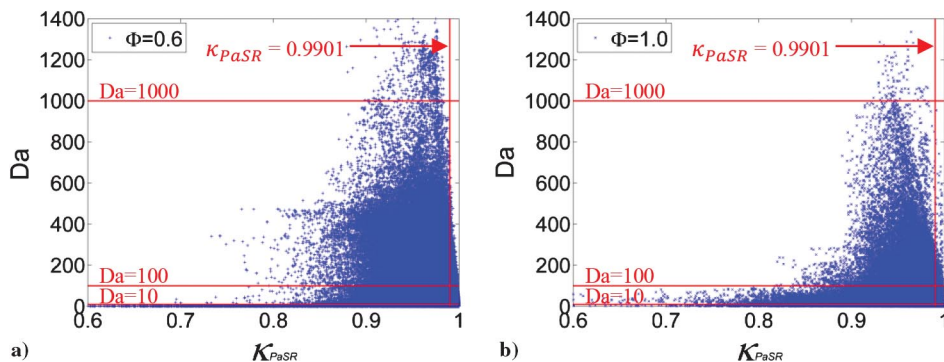

Fig. 19 Historic statistic of Da versus κ_{PaSR} for a) $\Phi = 0.6$ and b) 1.0.

Table 2   Statistics of the data point distributions in the Da-κ_{PaSR} diagram

κ_{PaSR}		$\leq 9.901 \times 10^{-3}$	$(9.901 \times 10^{-3}, 0.5]$	$(0.5, 0.9901]$	>0.9901
Da		$Ka < 0.01$	$Ka \in (0.01, 1]$	$Ka \in (1, 100]$	$Ka > 100$
≤ 1	$\Phi = 0.6$	0	0	0.006619	0.757855
	$\Phi = 1.0$	0	0	0.013785	0.683948
$(1, 10]$	$\Phi = 0.6$	0	7.7666×10^{-8}	0.057300	0.128544
	$\Phi = 1.0$	0	1.2334×10^{-7}	0.143695	0.103135
$(10, 100]$	$\Phi = 0.6$	0	0	0.025205	0.015837
	$\Phi = 1.0$	0	1.2334×10^{-7}	0.047021	0.005351
$(100, 1000]$	$\Phi = 0.6$	0	0	0.007539	0.001059
	$\Phi = 1.0$	0	0	0.002930	0.000122
>1000	$\Phi = 0.6$	0	0	4.0347×10^{-5}	0
	$\Phi = 1.0$	0	0	1.1964×10^{-5}	0

Note: Three combustion mode zones are divided by the bold lines: *upper*, slow chemistry zone; *bottom right*, thin reaction zone; *bottom left*, flamelet zone.
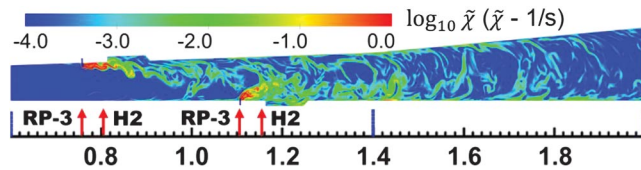
Fig. 20   Instantaneous contour of scalar dissipation rate in logarithmic scale for $\Phi = 1.0$.

characteristic diffusion time scale. Large values of the scalar dissipation rate mainly occur in the rim of fuel jet streams that are not completely mixing, and all fall into the 8-cm incomplete mixing distance in Fig. 11a since the mixture fraction distribution has a large gradient there. Because the fuel has not been perfectly mixed, those regions with high $\tilde{\chi}$ (>1 s^{-1}) have weak combustion reactions and generally correspond to the regions with a low heat release rate in Fig. 12b. For the main reaction regions, the scalar dissipation rate is even lower ($\ll 1$ s^{-1}), and thereby the characteristic diffusion time scale is overall much longer ($\gg 1$ s), compared with the convection time scale ($\sim o(1)$ ms) in the combustor flow path. The chemical equilibrium time can be approximated by the ignition time defined by the peak in CO concentration as shown in Fig. 2c. From 1200 to 2400 K, the equilibrium time varies from 3.2×10^{-3} to 4.7×10^{-6} s, which corresponds to a transferring distance of 32 cm to 4.7 mm, assuming a typical flow speed of 1000 m/s in the burner section. As seen, the time scale for equilibrium chemistry above 1200 K is comparable with the convection time scale, but much smaller than the diffusion time scale. This demonstrates that in supersonic flows the convection process has more influence on the reaction progress than the diffusion process. Actually, due to the slow chemistry of kerosene combustion, most of the reactions cannot be fully completed, that is, reaching an equilibrium status, within a single cell, but rather are transported downstream with incomplete products. Although the equilibrium time scale is of several orders shorter than the diffusion time scale when above 1200 K, once below 800 K the equilibrium time scale exceeds 1 s, and hence the scalar diffusion will exhibit a perceivable influence on the local reactions; that is, the reactants cannot be completely reacted before being dispersed by scalar diffusion.

V.   Conclusions

Improved delayed detached Eddy simulation modelings of a full-scale actively cooled scramjet combustor operated under two different kerosene/air ratios are conducted to reveal the combined flow, mixing, and combustion characteristics in the internal flow fields. The kerosene/air chemistry is modeled by a newly developed 28s/92r skeletal mechanism. A one-dimensional solid-gas-liquid coupling method is developed to simulate the active cooling effect. A reformulated PaSR is proposed to adapt it for high mesh resolution. The modeling results were validated against the measured pressure and wall heat flux, and overall good agreements are achieved using current modeling framework.

The supersonic flow, mixing, and combustion characteristics under the two fuel/air ratios are quantitatively compared based on the efficiency indices, Takeno Flame Index, and the correlation statistics between heat release rate and mixture fraction. As Φ increases, the mean Ma and the mean supersonic flux ratio decrease as expected. The mean supersonic flux ratio is larger than 34% over the whole streamwise flow path, indicating that the combustor runs in scramjet mode for both cases. The mean heat release distribution denotes that the flame stabilizes in cavity mode for the upstream fuel jet while in jet-wake mode for the downstream fuel jet. Efficiency indices show that the complete mixing is quick, the combustion reactions start earlier for the lower Φ, and the final combustion efficiency at the expander outlet rises again to a higher value of 84% for $\Phi = 0.6$ than the value of 78% for $\Phi = 1.0$. The total pressure loss is 23% higher at the higher Φ, but with lower initial values. The correlation statistics between heat release rate and mixture fraction shows that the pyrolysis and oxidation reactions are both intensified from the fuel-lean case to the stoichiometric case, the pyrolysis region and the peak heat release rate both appear a rich-shifting phenomenon, and a secondary peak for the heat release rate is observed. Most of endothermic reactions occur under the premixed mode, and the ratio of premixed mode decreases with the increasing of Φ.

The vorticity and its evolution are analyzed through the five source terms for the two cases. The mean vorticity and the mean supersonic-subsonic vorticity ratio are slightly higher for $\Phi = 1.0$ except at the initial shock impinging point. The total source term of vorticity almost doubles since the upstream fuel injection as Φ increases, and the overwhelming majority of the source term is generated in the subsonic regions. For both the examined supersonic kerosene combustion cases, the convection and the dilatational terms have the highest order of magnitude $\sim O(10^9)$ s^{-2}, the vortex stretching and the diffusion terms have the medium order of magnitude $\sim O(10^8)$ s^{-2}, and the baroclinic term has the lowest order of magnitude $\sim O(10^7)$ s^{-2}.

The turbulence-chemistry interaction is analyzed by the aid of numerous quantitative indices, such as Damköhler number, PaSR coefficient, and scalar dissipation rate, as well as their correlation statistics. The correlation diagram of Da versus κ_{PaSR} shows that Da peaks at $\kappa_{PaSR} = 0.95$ for the both cases, more data points occur with Da > 1000 for the fuel-lean (oxygen-rich) case, and the κ_{PaSR} spans to a lower value for $\Phi = 1.0$. Statistics shows that most of the data points, 95.03% for $\Phi = 0.6$ and 94.46% for $\Phi = 1.0$, are distributed in the slow chemistry zone, whereas only a small percentage, 4.97% for $\Phi = 0.6$ and 5.54% for $\Phi = 1.0$, are distributed in the thin reaction zone, and almost zero in the flamelet zone. Above 1200 K, the time scale for equilibrium chemistry is of several orders shorter than the diffusion time scale but comparable with the convection time scale.

Appendix: List of the reactions involved in the skeletal mechanism of kerosene-O_2 combustion (28 species and 92 steps) and coefficients for the calculation of rate constants

No.	Reaction	A	n	E
1.	$NC_{10}H_{22} \rightleftharpoons PC_4H_9 + AC_6H_{13}$	$2.000 \cdot 10^{17}$	0.00	83180.0
2.	$NC_{10}H_{22} \rightleftharpoons C_2H_5 + AC_8H_{17}$	$2.000 \cdot 10^{17}$	0.00	83680.0
3.	$IC_8H_{18} \rightleftharpoons TC_4H_9 + IC_4H_9$	$1.000 \cdot 10^{17}$	0.00	79000.0
4.	$PCH \rightarrow 3C_2H_4 + C_3H_6$	$1.300 \cdot 10^{17}$	0.00	84000.0
5.	$PCH \rightleftharpoons PCHE + H$	$6.000 \cdot 10^{15}$	0.00	99520.0
6.	$PCH + O_2 \rightleftharpoons PCHE + HO_2$	$1.400 \cdot 10^{13}$	0.00	49910.0
7.	$PCH + OH \rightleftharpoons PCHE + H_2O$	$1.100 \cdot 10^{13}$	0.00	790.0
8.	$PCH + H \rightleftharpoons PCHE + H_2$	$2.600 \cdot 10^{06}$	2.40	4471.0
9.	$PCH + O \rightleftharpoons PCHE + OH$	$1.100 \cdot 10^{06}$	2.50	2830.0
10.	$PCH + C_2H_3 \rightleftharpoons PCHE + C_2H_4$	$3.020 \cdot 10^{00}$	3.50	5481.0
11.	$PCH + HCO \rightleftharpoons PCHE + CH_2O$	$4.500 \cdot 10^{11}$	0.00	9540.0
12.	$C_2H_3 + O_2 \rightleftharpoons CH_2O + HCO$	$9.275 \cdot 10^{25}$	-3.96	7043.0
13.	$CH_3 + OH \rightleftharpoons CH_2O + H_2$	$7.390 \cdot 10^{14}$	-1.13	14551.0
14.	$H + H + M \rightleftharpoons H_2 + M$	$1.000 \cdot 10^{18}$	-1.0	0.0
	Third-body efficiencies: $H_2O = 16.25$; $CO = 1.875$; $CO_2 = 3.75$; $H_2 = 2.50$			
15.	$H + O_2 \rightleftharpoons OH + O$	$1.900 \cdot 10^{14}$	0.0	16812.0
16.	$H + O_2 + M \rightleftharpoons HO_2 + M$	$8.000 \cdot 10^{17}$	-0.80	0.0
	Third-body efficiencies: $H_2O = 16.25$; $CO = 1.875$; $CO_2 = 3.75$; $H_2 = 2.50$			
17.	$H + OH + M \rightleftharpoons H_2O + M$	$3.000 \cdot 10^{22}$	-2.0	0.0
	Third-body efficiencies: $H_2O = 16.25$; $CO = 1.875$; $CO_2 = 3.75$; $H_2 = 2.50$			
18.	$H_2 + O_2 \rightleftharpoons OH + OH$	$1.700 \cdot 10^{13}$	0.0	47780.0
19.	$O + H_2 \rightleftharpoons OH + H$	$1.30 \cdot 10^{04}$	2.80	5922.0
20.	$H2 + OH \rightleftharpoons H_2O + H$	$2.160 \cdot 10^{08}$	1.5	3430.0
21.	$O + O + M \rightleftharpoons O_2 + M$	$1.140 \cdot 10^{17}$	-1.0	0.0
	Third-body efficiencies: $H_2O = 16.25$; $CO = 1.875$; $CO_2 = 3.75$; $H_2 = 2.50$			
22.	$O + H + M \rightleftharpoons OH + M$	$6.200 \cdot 10^{16}$	-0.6	0.0
	Third-body efficiencies: $H_2O = 16.25$; $CO = 1.875$; $CO_2 = 3.75$; $H_2 = 2.50$			
23.	$H_2O + O \rightleftharpoons OH + OH$	$1.500 \cdot 10^{10}$	1.14	17260.0
24.	$HO_2 + OH \rightleftharpoons H_2O + O_2$	$1.450 \cdot 10^{13}$	0.0	-497.0
25.	$HO_2 + O \rightleftharpoons OH + O_2$	$2.440 \cdot 10^{13}$	0.0	-446.0
26.	$H + HO_2 \rightleftharpoons H_2 + O_2$	$2.140 \cdot 10^{13}$	0.0	1411.0
27.	$H + HO_2 \rightleftharpoons OH + OH$	$8.400 \cdot 10^{13}$	0.0	875.0
28.	$H + HO_2 \rightleftharpoons H_2O + O$	$3.010 \cdot 10^{13}$	0.0	1721.0
29.	$CO + HO_2 \rightleftharpoons CO_2 + OH$	$1.150 \cdot 10^{05}$	2.30	17550.0
30.	$CO + OH \rightleftharpoons CO_2 + H$	$4.400 \cdot 10^{06}$	1.50	-740.0
31.	$CO + O + M \rightleftharpoons CO_2 + M$	$2.830 \cdot 10^{13}$	0.0	-4540.0
	Third-body efficiencies: $H_2O = 16.25$; $CO = 1.875$; $CO_2 = 3.75$; $H_2 = 2.50$			
32.	$CO + O_2 \rightleftharpoons CO_2 + O$	$2.530 \cdot 10^{12}$	0.0	47700.0
33.	$HCO + M \rightleftharpoons H + CO + M$	$2.300 \cdot 10^{17}$	-1.0	17090.0
	Third-body efficiencies: $H_2O = 16.25$; $CO = 1.875$; $CO_2 = 3.75$; $H_2 = 2.50$			
34.	$HCO + OH \rightleftharpoons CO + H_2O$	$1.000 \cdot 10^{14}$	0.0	0.0
35.	$HCO + O \rightleftharpoons CO + OH$	$3.000 \cdot 10^{13}$	0.0	0.0
36.	$HCO + O \rightleftharpoons CO_2 + H$	$3.000 \cdot 10^{13}$	0.0	0.0
37.	$HCO + H \rightleftharpoons CO + H_2$	$7.220 \cdot 10^{13}$	0.0	0.0
38.	$HCO + O_2 \rightleftharpoons CO + HO_2$	$7.580 \cdot 10^{12}$	0.0	410.0
39.	$HCO + HO_2 \rightleftharpoons CO_2 + OH + H$	$3.000 \cdot 10^{13}$	0.0	0.0
40.	$HCO + HCO \rightleftharpoons CH_2O + CO$	$1.200 \cdot 10^{13}$	0.0	0.0
41.	$HCO + HCO \rightleftharpoons H_2 + CO + CO$	$3.000 \cdot 10^{12}$	0.0	0.0
42.	$CH_3 + O \rightleftharpoons H + CH_2O$	$8.430 \cdot 10^{13}$	0.0	0.0
43.	$CH_3 + O \rightarrow H + H_2 + CO$	$3.370 \cdot 10^{13}$	0.0	0.0
44.	$CH_3 + O_2 \rightleftharpoons CH_2O + OH$	$6.620 \cdot 10^{11}$	0.00	14188.0
45.	$CH_3 + CH_3 \rightleftharpoons C_2H_5 + H$	$3.010 \cdot 10^{13}$	0.0	13513.0
46.	$CH_2O + OH \rightleftharpoons HCO + H_2O$	$1.716 \cdot 10^{09}$	1.18	-447.0
47.	$CH_2O + M \rightleftharpoons HCO + H + M$	$5.850 \cdot 10^{14}$	0.00	64200.0
	Third-body efficiencies: $H_2O = 16.25$; $CO = 1.875$; $CO_2 = 3.75$; $H_2 = 2.50$			
48.	$CH_2O + O \rightleftharpoons HCO + OH$	$1.810 \cdot 10^{13}$	0.00	3088.0
49.	$CH_2O + H \rightleftharpoons HCO + H_2$	$1.100 \cdot 10^{08}$	1.80	3000.0
50.	$CH_2O + O_2 \rightleftharpoons HCO + HO_2$	$1.230 \cdot 10^{06}$	3.00	52000.0
51.	$C_2H_5 + OH \rightleftharpoons C_2H_4 + H_2O$	$2.409 \cdot 10^{13}$	0.00	0.0
52.	$C_2H_5 + OH \rightarrow CH_3 + CH_2O + H$	$2.409 \cdot 10^{13}$	0.00	0.0
53.	$C_2H_5 + O \rightleftharpoons CH_2O + CH_3$	$4.238 \cdot 10^{13}$	0.00	0.0
54.	$C_2H_5 + O \rightleftharpoons C_2H_4 + OH$	$3.046 \cdot 10^{13}$	0.00	0.0
55.	$C_2H_5 + H \rightleftharpoons C_2H_4 + H_2$	$1.250 \cdot 10^{14}$	0.00	8000.0
56.	$C_2H_4 + H(+M) \rightleftharpoons C_2H_5(+M)$	$3.973 \cdot 10^{09}$	1.283	1292.0
	LOW/$2.791 \cdot 10^{18}$ 0.00 755.0/			
	TROE/0.76 40.0 1025.0/			
57.	$C_2H_4 + H_2 \rightleftharpoons CH_3 + CH_3$	$3.767 \cdot 10^{12}$	0.83	84710.0
	REV/1.000E+140.00 3.200E+04/			
58.	$C_2H_4 + M \rightleftharpoons C_2H_3 + H + M$	$2.970 \cdot 10^{17}$	0.00	96560.0
	Third-body efficiencies: $H_2O = 16.25$; $CO = 1.875$; $CO_2 = 3.75$			
59.	$C_2H_4 + OH \rightleftharpoons C_2H_3 + H_2O$	$2.024 \cdot 10^{13}$	0.00	5936.0
60.	$C_2H_4 + O \rightleftharpoons CH_3 + HCO$	$1.200 \cdot 10^{08}$	1.44	530.0
61.	$C_2H_4 + H \rightleftharpoons C_2H_3 + H_2$	$1.000 \cdot 10^{14}$	0.00	15009.0

Appendix   (Continued.)

No.	Reaction	A	n	E
62.	$C_2H_4 + O_2 \rightleftharpoons C_2H_3 + HO_2$	$4.220 \cdot 10^{13}$	0.00	57629.0
63.	$C_2H_4 + C_2H_4 \rightleftharpoons C_2H_5 + C_2H_3$	$5.000 \cdot 10^{14}$	0.00	64700.0
64.	$C_2H_3 + HO_2 \rightarrow CH_3 + CO + OH$	$3.000 \cdot 10^{13}$	0.00	0.0
65.	$C_2H_3 + O \rightleftharpoons CH_3 + CO$	$1.500 \cdot 10^{13}$	0.00	0.0
66.	$C_2H_3 + HCO \rightleftharpoons C_2H_4 + CO$	$9.034 \cdot 10^{13}$	0.00	0.0
67.	$C_2H_3 + CH_2O \rightleftharpoons C_2H_4 + HCO$	$5.420 \cdot 10^{03}$	2.81	5862.0
68.	$IC_3H_7 \rightleftharpoons C_2H_4 + CH_3$	$1.140 \cdot 10^{11}$	0.00	31110.0
69.	$C_3H_6 + H(+M) \rightleftharpoons IC_3H_7(+M)$	$5.700 \cdot 10^{09}$	1.20	874.0
	LOW/$1.64 \cdot 10^{54} -11.109364.0/$			
	TROE/$1.01.0 \cdot 10^{-15}$ 260.0 3000.0/			
	Third-body efficiencies: $H_2O = 16.25$; $CO = 1.875$; $CO_2 = 3.75$			
70.	$IC_3H_7 + O_2 \rightleftharpoons C_3H_6 + HO_2$	$2.754 \cdot 10^{10}$	0.00	-2151.0
71.	$IC_3H_7 + H \rightleftharpoons C_2H_5 + CH_3$	$5.00 \cdot 10^{13}$	0.00	0.0
72.	$IC_3H_7 + H \rightleftharpoons C_3H_6 + H_2$	$3.614 \cdot 10^{12}$	0.00	0.0
73.	$C_3H_6 \rightleftharpoons C_2H_3 + CH_3$	$1.100 \cdot 10^{21}$	-1.20	97720.0
74.	$C_3H_6 + O \rightleftharpoons C_2H_5 + HCO$	$4.689 \cdot 10^{07}$	1.57	-628.0
75.	$C_3H_6 + O \rightleftharpoons C_2H_4 + CH_2O$	$7.020 \cdot 10^{07}$	1.57	-628.0
76.	$C_3H_6 + H \rightleftharpoons C_2H_4 + CH_3$	$7.230 \cdot 10^{12}$	0.00	1302.0
77.	$PC_4H_9 \rightleftharpoons C_2H_5 + C_2H_4$	$2.500 \cdot 10^{13}$	0.00	28824.0
78.	$PC_4H_9 \rightleftharpoons C_3H_6 + CH_3$	$1.260 \cdot 10^{12}$	0.00	27026.0
79.	$AC_6H_{13} \rightleftharpoons PC_4H_9 + C_2H_4$	$1.020 \cdot 10^{12}$	0.30	27276.0
80.	$AC_8H_{17} \rightleftharpoons AC_6H_{13} + C_2H_4$	$9.120 \cdot 10^{11}$	0.31	27240.5
81.	$IC_4H_9 \rightleftharpoons C_3H_6 + CH_3$	$2.000 \cdot 10^{13}$	0.0	29950.0
82.	$IC_4H_9 \rightleftharpoons IC_4H_8 + H$	$1.914 \cdot 10^{29}$	-5.246	39758.0
83.	$IC_4H_9 + O_2 \rightleftharpoons IC_4H_8 + HO_2$	$2.400 \cdot 10^{10}$	0.0	0.0
84.	$IC_4H_9 + HO_2 \rightarrow IC_3H_7 + CH_2O + OH$	$2.410 \cdot 10^{13}$	0.0	0.0
85.	$TC_4H_9 \rightleftharpoons IC_4H_8 + H$	$2.902 \cdot 10^{51}$	-11.53	52620.0
86.	$TC_4H_9 \rightleftharpoons C_3H_6 + CH_3$	$3.000 \cdot 10^{14}$	0.0	46300.0
87.	$TC_4H_9 + O_2 \rightleftharpoons IC_4H_8 + HO_2$	$5.000 \cdot 10^{11}$	0.0	2500.0
88.	$TC_4H_9 + OH \rightleftharpoons IC_4H_8 + H_2O$	$1.800 \cdot 10^{13}$	0.0	0.0
89.	$TC_4H_9 + H \rightleftharpoons IC_4H_8 + H_2$	$5.400 \cdot 10^{12}$	0.0	0.0
90.	$TC_4H_9 + O \rightleftharpoons IC_4H_8 + OH$	$4.160 \cdot 10^{14}$	0.0	0.0
91.	$IC_4H_8 + O \rightleftharpoons IC_3H_7 + HCO$	$0.500 \cdot 10^{09}$	1.28	-1079.0
92.	$IC_4H_8 + H \rightleftharpoons C_3H_6 + CH_3$	$1.720 \cdot 10^{13}$	0.0	3600.0

Note: 1) The rate constant is given by the Arrhenius formula $k = AT^b \exp(-E/RT)$; 2) when third-body reactions are involved, the rate constant is multiplied by the third-body concentration given as $[C_M] = \sum_{\alpha=1}^{L} \gamma_\alpha [C_\alpha]$, where γ_α is the third-body coefficient for species α; 3) TROE stands for the true pressure-dependent reaction rate, and LOW stands for the low-pressure limit for pressure-dependent unimolecular fall-off reactions, 4) REV denotes the reverse reaction parameters that supersede the reverse rates normally computed through the equilibrium constant; and 5) the default units for A are in cm, s, K, and mole.

References

[1] Liu, P., He, G., Hu, Z., and Zhang, M., "Large-Eddy Simulation of Kerosene Spray Combustion in a Model Scramjet Chamber," *Proceedings of the Institution of Mechanical Engineers, Part G: Journal of Aerospace Engineering*, Vol. 224, No. 9, 2010, pp. 949–960.
doi:10.1243/09544100JAERO738

[2] Kumaran, K., and Babu, V., "Mixing and Combustion Characteristics of Kerosene in a Model Supersonic Combustor," *Journal of Propulsion and Power*, Vol. 25, No. 3, 2009, pp. 583–592.
doi:10.2514/1.40140

[3] Kumaran, K., Behera, P. R., and Babu, V., "Numerical Investigation of the Supersonic Combustion of Kerosene in a Strut-Based Combustor," *Journal of Propulsion and Power*, Vol. 26, No. 5, 2010, pp. 1084–1091.
doi:10.2514/1.46965

[4] Fureby, C., Chapuis, M., Fedina, E., and Karl, S., "CFD Analysis of the Hyshot II Scramjet Combustor," *Proceedings of the Combustion Institute*, Vol. 33, No. 2, 2011, pp. 2399–2405.
doi:10.1016/j.proci.2010.07.055

[5] David, P., Erik, T., and Graham, C., "Hybrid Reynolds-Averaged and Large-Eddy Simulation of Scramjet Fuel Injection," AIAA Paper 2011-2344, 2011.
doi:10.2514/6.2011-2344

[6] Shur, M. L., Spalart, P. R., Strelets, M. K., and Travin, A. K., "A Hybrid RANS-LES Approach with Delayed-DES and Wall-Modelled LES Capabilities," *International Journal of Heat and Fluid Flow*, Vol. 29, No. 6, 2008, pp. 1638–1649.
doi:10.1016/j.ijheatfluidflow.2008.07.001

[7] Weller, H. G., Tabor, G., Jasak, H., and Fureby, C., "A Tensorial Approach to CFD Using Object Oriented Techniques," *Computers in Physics*, Vol. 12, No. 6, 1998, pp. 620–631.
doi:10.1063/1.168744

[8] Kee, R. J., Rupley, F. M., and Miller, J. A., "Chemkin-II: A Fortran Chemical Kinetics Package for the Analysis of Gas-Phase Chemical Kinetics," Sandia National Laboratories, Technical Rept. SAND89-8009B, 1989.

[9] Pope, S. B., "Computationally Efficient Implementation of Combustion Chemistry Using in Situ Adaptive Tabulation," *Combustion Theory and Modeling*, Vol. 1, No. 1, 1997, pp. 41–63.
doi:10.1080/713665229

[10] Kurganov, A., and Tadmor, E., "New High-Resolution Central Schemes for Nonlinear Conservation Laws and Convection–Diffusion Equations," *Journal of Computational Physics*, Vol. 160, No. 1, 2000, pp. 241–282.
doi:10.1006/jcph.2000.6459

[11] Greenshields, C. J., Weller, H. G., Gasparini, L., and Reese, J. M., "Implementation of Semi-Discrete, Non-Staggered Central Schemes in a Colocated, Polyhedral, Finite Volume Framework, for High-Speed Viscous Flows," *International Journal for Numerical Methods in Fluids*, Vol. 38, No. 2, 2009, pp. 139–161.
doi:10.1002/fld.2069

[12] Wu, K., Li, X., Yao, W., and Fan, X., "Three-Dimensional Numerical Study of the Acoustic Properties of a Highly Underexpanded Jet," AIAA Paper 2015-3572, 2015.
doi:10.2514/6.2015-3572

[13] Li, X., Wu, K., Yao, W., and Fan, X., "A Comparative Study of Highly Underexpanded Nitrogen and Hydrogen Jets Using Large Eddy Simulation," AIAA Paper 2015-3573, 2015.
doi:10.2514/6.2015-3573

[14] Li, X., Yao, W., and Fan, X., "Large-Eddy Simulation of Time Evolution and Instability of Highly Underexpanded Sonic Jets," *AIAA Journal*, Vol. 54, No. 10, 2016, pp. 3191–3211.
doi:10.2514/1.J054689

[15] Yao, W., Wang, J., Lu, Y., Li, X., and Fan, X., "Full-Scale Detached Eddy Simulation of Kerosene Fueled Scramjet Combustor Based on Skeletal Mechanism," AIAA Paper 2015-3579, 2015.
doi:10.2514/6.2015-3579

[16] Wu, K., Zhang, P., Yao, W., and Fan, X., "Numerical Investigation on Flame Stabilization in DLR Hydrogen Supersonic Combustor with Strut Injection," *Combustion Science and Technology*, Vol. 189, No. 12, 2017, pp. 2154–2179.
doi:10.1080/00102202.2017.1365847

[17] Yao, W., Yuan, Y., Li, X., Wang, J., Wu, K., and Fan, X., "Comparative Study of Elliptic and Round Scramjet Combustors Fueled by RP-3," *Journal of Propulsion and Power*, Nov. 2017, pp. 1–15.
doi:10.2514/1.B36721

[18] Bird, R. B., Stewart, W. E., and Lightfoot, E. N., *Transport Phenomena*, 2nd ed., Wiley, New York, 2002, p. 27.

[19] Spalart, P. R., and Allmaras, S. R., "A One-Equation Turbulence Model for Aerodynamic Flows," AIAA Paper 1992-0439, 1992.
doi:10.2514/6.1992-439

[20] Golovitchev, V. I., Nordin, N., Jarnicki, R., and Chomiak, J., "3-D Diesel Spray Simulations Using a New Detailed Chemistry Turbulent Combustion Model," SAE Technical Paper 2000-01-1891, 2000.
doi:10.4271/2000-01-1891

[21] Chomiak, J., and Karlsson, A., "Flame Liftoff in Diesel Sprays," *Symposium (International) on Combustion*, Vol. 26, No. 2, 1996, pp. 2557–2564.
doi:10.1016/S0082-0784(96)80088-9

[22] Chomiak, J., and Karlsson, A., "Physical and Chemical Effects in Diesel Spray Ignition," *Proceedings of the 21st International Congress on Combustion Engines*, International Council on Combustion Engines (CIMAC), London, May 1995, Paper D01.

[23] Fureby, C., "LES for Supersonic Combustion," AIAA Paper 2012-5979, 2012.
doi:10.2514/6.2012-5979

[24] Anderson, J. D., "Inviscid High-Temperature Nonequilibrium Flows," *Hypersonic and High-Temperature Gas Dynamics*, 2nd ed., AIAA, Reston, VA, 2006, p. 673.

[25] Dagaut, P., Karsenty, F., Dayma, G., Diévart, P., Hadj-Ali, K., Mzé-Ahmed, A., Braun-Unkhoff, M., Herzler, J., Kathrotia, T., and Kick, T., et al., "Experimental and Detailed Kinetic Model for the Oxidation of a Gas to Liquid (GtL) Jet Fuel," *Combustion and Flame*, Vol. 161, No. 3, 2014, pp. 835–847.
doi:10.1016/j.combustflame.2013.08.015

[26] Niemeyer, K. E., Sung, C.-J., and Raju, M. P., "Skeletal Mechanism Generation for Surrogate Fuels Using Directed Relation Graph with Error Propagation and Sensitivity Analysis," *Combustion and Flame*, Vol. 157, No. 9, 2010, pp. 1760–1770.
doi:10.1016/j.combustflame.2009.12.022

[27] Fan, X., and Yu, G., "Analysis of Thermophysical Properties of Daqing RP-3 Aviation Kerosene," *Journal of Propulsion Technology*, Vol. 27, No. 2, 2006, pp. 187–192.

[28] Lu, Y., Wang, X., Li, L., Cheng, D., Yao, W., and Fan, X., "Development and Preliminary Validation of a Thermal Analysis Method for Hydrocarbon Regenerative-Cooled Supersonic Combustor," AIAA Paper 2015-3556, 2015.
doi:10.2514/6.2015-3556

[29] Cheng, D., Wang, J., Gong, J., Lu, Y., Yao, W., Li, L., and Fan, X., "Measurement of Heat Flux Distribution of Supercritical Kerosene Fueled Supersonic Combustor," AIAA Paper 2016-4112, 2016.
doi:10.2514/6.2016-4112

[30] Kumaran, K., and Babu, V., "Investigation of the Effect of Chemistry Models on the Numerical Predictions of the Supersonic Combustion of Hydrogen," *Combustion and Flame*, Vol. 156, No. 4, 2009, pp. 826–841.
doi:10.1016/j.combustflame.2009.01.008

[31] Yamashita, H., Shimada, M., and Takeno, T., "A Numerical Study on Flame Stability at the Transition Point of Jet Diffusion Flames," *Proceeding of the Combustion Institute*, Vol. 26, No. 1, 1996, pp. 27–34.
doi:10.1016/S0082-0784(96)80196-2

[32] Niklas, Z., Kevin, N.-B., and Christer, F., "Understanding Scramjet Combustion Using LES of the Hyshot II Combustor," AIAA Paper 2015-3615, 2015.
doi:10.2514/6.2015-3615

[33] Law, C. K., Makino, A., and Lu, T. F., "On the Off-Stoichiometric Peaking of Adiabatic Flame Temperature," *Combustion and Flame*, Vol. 145, No. 4, 2006, pp. 808–819.
doi:10.1016/j.combustflame.2006.01.009

[34] You, Y., Ludeke, H., and Hannemann, K., "On the Flow Physics of a Low Momentum Flux Ratio Jet in a Supersonic Turbulent Crossflow," *Europhysics Letters*, Vol. 97, No. 2, 2012, Paper 24001.
doi:10.1209/0295-5075/97/24001

[35] Cecere, D., Ingenito, A., Giacomazzi, E., Romagnosi, L., and Bruno, C., "Hydrogen/Air Supersonic Combustion for Future Hypersonic Vehicles," *International Journal of Hydrogen Energy*, Vol. 36, No. 18, 2011, pp. 11969–11984.
doi:10.1016/j.ijhydene.2011.06.051

[36] Seiner, J. M., Dash, S. M., and Kenzakowski, D. C., "Historical Survey on Enhanced Mixing in Scramjet Engines," *Journal of Propulsion and Power*, Vol. 17, No. 6, 2001, pp. 1273–1286.
doi:10.2514/2.5876

[37] Ingenito, A., and Bruno, C., "Physics and Regimes of Supersonic Combustion," *AIAA Journal*, Vol. 48, No. 3, 2010, pp. 515–525.
doi:10.2514/1.43652

[38] Pera, C., Reveillon, J., Vervisch, L., and Domingo, P., "Modeling Subgrid Scale Mixture Fraction Variance in LES of Evaporating Spray," *Combustion and Flame*, Vol. 146, No. 4, 2006, pp. 635–648.
doi:10.1016/j.combustflame.2006.07.003

J. C. Oefelein
Associate Editor